Title: **Intestinal progenitor P-bodies maintain stem cell identity by suppressing pro-differentiation factors.**

Authors: Kasun Buddika[1], Yi-Ting Huang[1], Alex Butrum-Griffith[*1], Sam A. Norrell[*1], Alex M. O'Connor[*1], Viraj K. Patel[*1], Samuel A. Rector[*1], Mark Slovan[*1], Mallory Sokolowski[*1], Yasuko Kato[2], Akira Nakamura[3], Nicholas S. Sokol[1]

Affiliation: [1]Department of Biology, Indiana University, Bloomington, IN 47405, USA, [2]Advanced Insect Research Promotion Center, Kyoto Institute of Technology, Matsugasaki, Sakyo-ku, Kyoto, 606-8585, Japan, [3] Department of Germline Development, Institute of Molecular Embryology and Genetics, Kumamoto University, 2-2-1 Honjo, Kumamoto 860-0811, Japan

*** denotes equal contribution**

Correspondence: nsokol@indiana.edu (email)
812-856-6812 (phone)

Running Title: The structure and function of P-bodies in intestinal stem cells

Abstract

Post-transcriptional gene regulatory mechanisms allow cells to quickly respond to environmental variation without relying on nascent transcription. However, the role of these mechanisms in cell fate transitions in adult stem cell populations remain poorly understood. We address this question here by investigating the role of Processing bodies (P-bodies), a key site of post-transcriptional control, in adult *Drosophila* intestinal stem cells. We report that this cell type, but not surrounding differentiated cells, harbor P-bodies that contain *Drosophila* orthologs of mammalian P-body components DDX6, EDC3, EDC4 and LSM14A/B and are ultrastructurally organized in a “core-shell” structure. A targeted RNAi screen identified 100+ genes that affect normal P-body morphology including *patr-1*, which is required for mature P-body assembly. Using both verified *patr-1* RNAi strains and newly generated *patr-1* loss-of-function alleles, we show that P-body assembly defects correlate with loss of intestinal progenitors. RNA-seq analysis found that *patr-1* mutant progenitors inappropriately express enterocyte (EC)-specific genes, leading to precocious EC differentiation. We further demonstrate that this process is independent of well-known transcriptional repressor *escargot*, indicating P-body-dependent post-transcriptional regulation of pro-differentiation genes. Taken together, this work delineates the importance of post-transcriptional mechanisms in adult stem cell maintenance.

Introduction

In eukaryotic cells, translationally inactive messenger RNAs (mRNAs) can assemble to form a distinct population of cytoplasmic messenger ribonucleoprotein (mRNP) particles known as Processing bodies (P-bodies) (Anderson and Kedersha, 2006; Decker and Parker, 2012; Kedersha et al., 2005). Like stress granules, which are another class of mRNPs that form in cells experiencing extracellular stresses, P-bodies: [1] lack a limiting membrane and are visible via conventional microscopic techniques (Anderson and Kedersha, 2006), [2] are enhanced or induced by blocking translation initiation (Buchan and Parker, 2009; Chan et al., 2018; Franks and Lykke-Andersen, 2008; Kedersha et al., 2000; Teixeira et al., 2005), [3] are disassembled when treated with cycloheximide, a chemical that traps mRNAs on ribosomes (Anderson and Kedersha, 2009; Buchan and Parker, 2009; Kedersha et al., 2000; Mugler et al., 2016; Teixeira et al., 2005), and [4] are conserved from yeast to humans (Martínez et al., 2013; Protter and Parker, 2016). Unlike stress granules, however, P-bodies are constitutive and are known to contain proteins involved in mRNA decay (Anderson and Kedersha, 2006; Anderson and Kedersha, 2009; Buchan and Parker, 2009; Decker and Parker, 2012; Eulalio et al., 2007b; Luo et al., 2018; Parker and Sheth, 2007; Sheth and Parker, 2003; Youn et al., 2019). While recent studies have identified stress granules in adult tissues (Anderson et al., 2018; Buddika et al., 2020b; Gareau et al., 2013; Jevtov et al., 2015), whether P-bodies are also present in adult tissues and, if so, what biological processes they might control is not very well understood.

Investigation of the localization of 5'-to-3' mRNA decay machinery proteins paved the path to the discovery of P-bodies (Anderson and Kedersha, 2006; Bashkirov et al., 1997; Dijk et al., 2003; Eystathioy et al., 2003; Ingelfinger et al., 2002; Luo et al., 2018; Sheth and Parker, 2003; van Dijk et al., 2002). More recent fluorescent-activated particle sorting (FAPS) followed by liquid chromatography-tandem mass spectrometry (LC-MS/MS) identified 125 proteins to be abundantly present in sorted P-bodies from HEK293 cells (Hubstenberger et al., 2017). Identified P-body resident proteins include translation repression and mRNA decay factors (4E-T, LSM14A, LSM14B and IGF2BP2), microRNA pathway components (AGO1, AGO2 and MOV10), decapping complex proteins (DCP1A, DCP1B, DCP2 and EDC4) and nonsense-mediated mRNA

80 decay (NMD) factors (UPF1) (Hubstenberger et al., 2017). Twenty-eight of these P-
81 body proteins were also identified in the proteome of stress granule cores
82 (Hubstenberger et al., 2017; Jain et al., 2016; Youn et al., 2019), showing that proteins
83 are redundantly localized to both types of cytoplasmic granules. However, a more
84 recent systematic BioID approach identified a set of 38 proteins to be uniquely present
85 in P-bodies (Youn et al., 2019). FAPS-based P-body purification also identified 6,168
86 transcripts to be significantly enriched in P-bodies and another 7,588 transcripts that
87 were significantly depleted (Hubstenberger et al., 2017). This clear bifurcation of
88 resident mRNAs indicated that the P-body transcriptome is large but specific
89 (Hubstenberger et al., 2017; Standart and Weil, 2018). While its protein composition
90 suggested that the primary function of P-bodies was mRNA degradation (Anderson and
91 Kedersha, 2006; Decker and Parker, 2012), recent studies have found that mRNAs
92 localized to P-bodies can return to the cytoplasm to re-enter translation (Bhattacharyya
93 et al., 2006; Brengues et al., 2005) and that P-bodies can be disrupted without affecting
94 mRNA decay (Eulalio et al., 2007b; Stoecklin et al., 2006). Therefore, current models
95 propose that P-bodies coordinate the storage of mRNA regulons leading to
96 stoichiometric protein production (Standart and Weil, 2018). However, further
97 experiments are necessary to better understand the role of P-bodies in eukaryotic cells.
98 Furthermore, while extensive super-resolution microscopy has revealed that stress
99 granules have a core-shell structure, where the core is stable and the more dynamic
100 shell allows mRNAs and proteins to shuttle between the granule and the cytoplasm
101 (Jain et al., 2016; Niewidok et al., 2018; Wheeler et al., 2016), similar super-resolution
102 characterizations are necessary to elucidate whether P-bodies also possess a specific
103 structural organization (Youn et al., 2019).
104 Recent findings suggest that post-transcriptional mechanisms are critical for
105 maintaining proper stem cell functions. Although post-transcriptional processes such as
106 alternative splicing, polyadenylation, and RNA modifications are extensively studied in
107 pluripotent stem cells such as embryonic stem cells (ESCs) (Batista et al., 2014; Bertero
108 et al., 2018; Brumbaugh et al., 2018; Conway et al., 2016; Guallar et al., 2018; Han et
109 al., 2013; Lackford et al., 2014; Lu et al., 2013; Wilbert et al., 2012; Yeo et al., 2009),
110 other RNA processes such as RNA decay, storage and translational control remain

111 poorly understood (Chen et al., 2015; Di Stefano et al., 2019; Luhur et al., 2017; Wang
112 et al., 2015). Interestingly, recent work suggests that the role of P-bodies in adult stem
113 cells is likely to be complex and dynamic: functional analysis of the P-body protein
114 DDX6 found that it promotes differentiation in some *in vitro* derived stem cell lineages
115 and represses it in others (Di Stefano et al., 2019). Thus, tissue-based stem cell models
116 will be critical for probing P-body function in an *in vivo* context. The intestinal epithelium
117 of adult *Drosophila* offers such a model to study post-transcriptional gene regulatory
118 mechanisms (Buddika et al., 2020b; Chen et al., 2015; Luhur et al., 2017). This actively
119 regenerating tissue hosts a population of progenitor cells, which is composed of two
120 main cell types: mitotic intestinal stem cells (ISCs) and their transient and non-mitotic
121 daughters, enteroblasts (EBs), that are primed for differentiation (Micchelli and
122 Perrimon, 2006; Ohlstein and Spradling, 2006). In this study, we find that *Drosophila*
123 orthologs of mammalian P-body components, DDX6, EDC3, EDC4 and LSM14A/B are
124 enriched and colocalized to form mature P-bodies in these intestinal progenitor cells.
125 Although P-bodies were readily detected in progenitor cells, similar structures were
126 absent in their neighboring terminally differentiated cells. By analyzing the function of
127 PATR-1, an evolutionary conserved RNA-binding protein that functions in both
128 translational repression and mRNA decay (Pilkington and Parker, 2008; Teixeira and
129 Parker, 2007) and is necessary for mature P-body assembly, we find that loss of P-
130 bodies leads to progressive progenitor cell loss due to enhanced ISC-to-EC
131 differentiation. Therefore, we propose that intestinal progenitor P-bodies are necessary
132 for stem cell maintenance by repressing the expression of pro-differentiation factors.
133

134 ## Results

135

136 **P-body components are enriched in intestinal progenitor cells**

137 Because intestinal progenitor cells contain a robust population of stress granules,
138 (Buddika et al., 2020b), we investigated whether they also contain P-bodies, a second
139 class of mRNPs that play vital roles in post-transcriptional gene regulation (Anderson
140 and Kedersha, 2006; Eulalio et al., 2007a; Eulalio et al., 2007b; Sheth and Parker,
141 2003). To test this possibility, we stained intestines of wildtype, 7-day old, adult female
142 *Drosophila* reared under standard conditions using a series of antibodies. This series
143 included faithful P-body markers such as EDC3, GE-1 (known in metazoans as EDC4),
144 Me31B (known in metazoans as DDX6), and TRAL (known in metazoans as LSM14A)
145 (Anderson and Kedersha, 2006; Ayache et al., 2015; Eulalio et al., 2007b;
146 Hubstenberger et al., 2017). We used previously published and verified antibodies
147 (Barbee et al., 2006; Fan et al., 2011; Nakamura A, Amikura R, Hanyu K, 2001) to
148 detect all of these proteins except for TRAL and EDC3, for which we generated and
149 validated new antibodies (**Fig. S1A-B**). Similar to what we observed with stress granule
150 proteins, these P-body proteins displayed elevated signal in intestinal progenitors (**Fig.
151 1A-D**), which are marked by horseradish peroxidase (HRP) (O'Brien et al., 2011). While
152 being limited to the cytoplasm, confocal microscopy detected these proteins in clearly
153 separated cytoplasmic granules (**Fig. 1A''-D''**). The staining pattern was similar in level
154 and cytoplasmic organization in both ISCs and *3Xgbe-smGFP::V5::nls* positive EBs
155 (**Fig. 1A''-D''**, compare staining of the cell marked with yellow * to the unmarked cell).
156 We also co-stained intestines with TRAL and Me31B to evaluate their relative
157 distribution and found that TRAL and Me31B granules perfectly overlapped, indicating
158 colocalization of P-body components under standard growth conditions (**Fig. 1E-E'**).
159 The apparent enrichment of P-body proteins in HRP^+ intestinal progenitors relative to
160 neighboring polyploid ECs indicated that these proteins were downregulated during EC
161 differentiation (see **Fig. 1A-E** and **Fig. S2A-B**). To assess the expression of P-body
162 protein in EEs, we stained dissected intestines with PROS, a marker for EEs (Micchelli
163 and Perrimon, 2006) and either TRAL or Me31B. The majority of EEs showed very low
164 to no detectable staining (**Fig. S2A-B**), suggesting P-body proteins were downregulated

165 in the EE lineage as well, although TRAL or Me31B levels were comparable to
166 progenitors in ~20% of EEs. Taken together, these data indicated the presence of a
167 population of cytoplasmic granules containing colocalized P-body components in
168 progenitor cells that were cleared during EC or EE differentiation.
169
170 **P-bodies and stress granules are distinct mRNPs in progenitor cells**
171 We previously showed that stress granule proteins form an intricate network of
172 stable mRNPs, which function as cores during the formation of mature intestinal
173 progenitor stress granules (IPSGs) in response to stress (Buddika et al., 2020b). To
174 rigorously compare the cytoplasmic locations of P-body proteins with IPSG proteins
175 under control and stressed conditions, we turned to structured illumination super-
176 resolution microscopy (SIM). We treated intestines *ex-vivo* with rapamycin prepared in
177 Krebs Ringer Bicarbonate Buffer (KRB) to induce stress and, in parallel, we treated
178 control intestines with only KRB for the same length of time. We first compared the size
179 distribution of stress granule component FMRP with P-body component TRAL.
180 Consistent with our previous report (Buddika et al., 2020b), the average area of FMRP
181 granules increased ~3.7-fold after rapamycin treatment (0.026 μm^2 [n=629 puncta, 8
182 cells] after KRB treatment; 0.097 μm^2 [n=657 puncta, 25 cells] after rapamycin
183 treatment) (**Fig. 2A, C**, **E**). In comparison, TRAL granules were ~1.8-fold larger than
184 FMRP mRNPs under control conditions, but grew to roughly the same size as FMRP+
185 IPSGs after rapamycin treatment (0.047 μm^2 [n=804 puncta, 14 cells] after KRB
186 treatment; 0.098 μm^2 [n=1215 puncta, 42 cells] after rapamycin treatment) (**Fig. 2B**, **D**
187 ,**E**). Indeed, no statistical difference was observed between the average area of FMRP
188 IPSGs or TRAL granules following rapamycin treatment (**Fig 2E**). These quantitative
189 data indicated that TRAL+ P-bodies were distinct from FMRP+ mRNPs under non-
190 stressed conditions, and that stress led to the enlargement of these mRNPs into IPSGs.
191 To qualitatively compare P-body and IPSG markers, we used SIM to compare
192 the expression pattern of one IPSG component (HA-tagged RIN (RIN::HA)) and one P-
193 body component (TRAL) under both control and stressed conditions. For comparison,
194 we also analyzed the distribution of two IPSG components (FMRP and RIN::HA) relative
195 to one another, as well as two P-body components (TRAL and Me31B) relative to one

196 another under these same conditions. Consistent with previously published data
197 (Buddika et al., 2020b), the two IPSG proteins, FMRP and RIN::HA, showed distinct but
198 partially overlapping patterns of small dots (Pearson's r value 0.33) in progenitor
199 cytoplasm under control conditions (**Fig. 2F-F', G**). However, FMRP and RIN::HA
200 signals were almost entirely overlapping (Pearson's r value 0.84) after rapamycin
201 treatment (**Fig. 2H-H'**, **I**). A similar relationship was observed with TRAL and RIN::HA,
202 which displayed distinct though partially overlapping foci (Pearson's r value 0.17) in the
203 control, but almost entirely overlapping larger foci (Pearson's r value 0.71) after stress
204 (**Fig. 2J-J', L-L'**, **K, M**). Given that larger RIN::HA foci represent IPSGs after rapamycin
205 treatment (Buddika et al., 2020b), this result indicates that P-body proteins localized to
206 mature IPSGs due to acute stresses. Unlike IPSG proteins, the two P-body proteins,
207 TRAL and Me31B, overlapped equally well with one another under both control
208 (Pearson's r value 0.90) and stressed (Pearson's r value 0.89) conditions (**Fig. 2N-N',**
209 **P-P'**, **O, Q**). Furthermore, while mature IPSGs can have irregular shapes, P-bodies tend
210 to have a regular spherical organization (compare **Fig. 2H', L', P'** granule appearance
211 to **J'-N'**). Based on this detailed quantitative and qualitative characterization, we
212 concluded that P-bodies are a second population of mRNPs in intestinal progenitors of
213 adult *Drosophila*.
214 Compared to stress granules, which contain a well-studied core-shell structure,
215 the structural organization of P-bodies is not well understood (Protter and Parker, 2016;
216 Wheeler et al., 2016; Youn et al., 2019). Therefore, we used the intestinal progenitor P-
217 body system to assess the ultrastructural organization within a mature P-body. First, we
218 stained dissected intestines with either Me31B, TRAL or EDC3 and then imaged the
219 cytoplasmic distribution of these proteins using SIM. Next, we used the FIJI package of
220 ImageJ to generate intensity maps of each protein. Close inspection of globular
221 granules revealed that the distribution of Me31B, TRAL or EDC3 was not uniform within
222 a granule (**Fig. 2R, T, V**). We noted that the pixel density was different along the length
223 of a granule and certain domains within the granule contained more protein
224 accumulation than the rest of the granule (**Fig. 2S, U, W**). Given that this non-uniform
225 protein organization within mature P-bodies is very similar to the core-shell organization
226 of a stress granule, we propose that P-bodies share the same structural organization.

227 Although significantly smaller, P-bodies are likely to have multiple cores similar to stress
228 granules (**Fig. 2R-W**). Taken together, these data identified the existence of a
229 structurally organized population of steady-state P-bodies in intestinal progenitors of
230 adult *Drosophila*.
231
232 **Identification of genetic modifiers of progenitor P-bodies using a targeted screen**
233 To begin to define the genetic framework governing P-body formation in
234 progenitor cells, we performed a targeted genetic screen to identify genes that altered
235 P-body morphology. We specifically focused on genes implicated in RNA-related
236 processes, since P-bodies are known to be involved in RNA regulation in a range of
237 species, from yeast to mammals (Anderson and Kedersha, 2006; Eulalio et al., 2007a;
238 Luo et al., 2018), and generated a list of 600 candidate genes by using the GO term
239 analysis function on Flybase (http://flybase.org/) (**Table S2**). We focused on the 485
240 genes with Bloomington *Drosophila* Stock Center (https://bdsc.indiana.edu/) RNAi
241 strains to conduct a primary screen, and used TRAL as the P-body marker to score for
242 P-body morphology (**Fig. 3A**). We screened a total of 735 RNAi strains that targeted
243 these 485 genes: 186 genes were targeted using two or more RNAi strains, and the
244 remainder were targeted by just one RNAi line. Individual RNAi strains were crossed to
245 a conditional version of *esg*-Gal4 (*esgTS*) (Micchelli and Perrimon, 2006), which
246 allowed us to specifically knock-down each gene in intestinal progenitors at the adult
247 stage, and dissected seven days post-RNAi. From this analysis, we identified 103
248 genes that affected TRAL granule morphology or expression. We classified these genes
249 into five phenotypic classes based on TRAL staining pattern: [1] large TRAL puncta
250 ("Big), [2] small TRAL puncta ("Small"), [3] dispersed TRAL puncta ("Diffuse), [4] both
251 dispersed and large TRAL puncta ("Diffuse + Big"), and [5] no TRAL staining ("No
252 TRAL") (**Fig. 3B**, representative images **Fig. 3E-J**, **Table S3-S4**). Consistent with P-
253 body function, the majority of positive genes were implicated in biological processes
254 such as mRNA catabolism and processing and were known components of cytoplasmic
255 ribonucleoprotein complexes, including P-bodies (**Fig. 3C-D**). For example, the
256 targeting of genes encoding P-body resident proteins EDC3 or PCM, the *Drosophila*
257 homolog of mammalian 5'-3' exonuclease XRN1, led to bigger TRAL granules.

258 Unexpectedly, a relatively large number of regulators of nuclear processes such as
259 RNA splicing and nuclear export as well as components of nuclear structures such as
260 the exon-exon junction complex (EJC) also impacted the morphology of cytoplasmic
261 TRAL granules (**Fig. 3C-D**, **Table S4**). To assess the specificity of these effects on P-
262 body morphology, a representative set of 25 positives -- 13 “big” genes, 3 “small” genes,
263 4 “diffuse” genes, 3 “diffuse + big” genes, and 2 “no TRAL” genes -- were also co-
264 stained with IPSG-makers FMRP and ROX8 (**Fig. 3K-P**, **Table S3**). While most had no
265 discernable effect, two genes, *fne* and CG13928, altered the expression profile of these
266 IPSG proteins and led to “big” or “diffuse and big” FMRP/ROX8 foci, respectively (**Table**
267 **S3**, **Fig. 3O**). Taken together, this targeted genetic screen identified a series of genes
268 that affected proper P-body organization or expression. Strikingly, 24% of these positive
269 genes displayed clear progenitor cell loss, suggesting that P-bodies facilitated
270 progenitor cell maintenance under standard growth conditions.
271
272 **PATR-1 is a P-body resident protein that is necessary for their formation**
273 Of the five phenotypic classes, we focused on the “diffuse” class because this
274 class interfered with TRAL granule assembly without apparently affecting TRAL protein
275 level. Among the six genes in this class, we focused on *patr-1*, which was previously
276 shown to act as a critical nucleator of P-bodies in yeast to mammalian cells (Coller and
277 Parker, 2005; Nissan et al., 2010; Pilkington and Parker, 2008; Pradhan et al., 2012;
278 Sachdev et al., 2019; V et al., 2011). First, to assess whether PATR-1 is expressed in
279 intestinal cells, we stained intestines of wildtype, 7-day old, adult female *Drosophila*
280 reared under standard conditions with a previously verified PATR-1 antibody (Pradhan
281 et al., 2012). Consistent with other P-body components (**Fig. 1**), PATR-1 antibody
282 displayed a clear elevated staining in HRP^+ intestinal progenitors (**Fig. 4A-B**).
283 Furthermore, similar to other progenitor P-body proteins, the progenitor staining was
284 almost exclusively detected in the cytoplasm and displayed a distinctive granular
285 organization (**Fig. 4B**). In contrast to TRAL and Me31B, PATR-1 also showed a strong
286 but less punctate expression in a subpopulation of EEs (compare **Fig. S2A-B** to **Fig.**
287 **4A, C**). To assess whether PATR-1 colocalized with progenitor P-bodies, we
288 simultaneously examined the cytoplasmic distribution of PATR-1 and TRAL or Me31B

289 using SIM. As expected, PATR-1 colocalized well with both progenitor P-body
290 components (**Fig. 4D-E** and quantified in **G-H**). Consistent with other P-body
291 components, PATR-1 did not colocalize with the IPSG protein FMRP (**Fig. 4F** and
292 quantified in **I**), and appeared to be in larger foci than FMRP granules (compare red and
293 green granule sizes in **Fig. 4F'**) under standard growth condition. In addition, we re-
294 screened the 103 genes that had altered TRAL expression or granule morphology for
295 effects on PATR-1 expression. We found that the effect on PATR-1 was analogous to
296 TRAL in all cases except for the "No TRAL" category, in which we observed smaller
297 than normal PATR-1 granules, suggesting that the identified genes altered overall P-
298 body morphology rather than specifically just TRAL staining (**Fig. 3Q-V**, **Table S3**).
299 Collectively, these data indicated that PATR-1 is a P-body component in intestinal
300 progenitor cells of adult *Drosophila*.
301 Since our screen indicated that TRAL granules failed to assemble in the absence
302 of PATR-1, we next asked whether knockdown of *patr-1* had a similar effect on other P-
303 body components. First, to evaluate the efficiency of the *patr-1* RNAi strain, we stained
304 control and *patr-1* RNAi intestines with the PATR-1 antibody. While PATR-1 granules
305 were detected in control intestinal progenitors, no signal was detected in progenitor cells
306 after *patr-1* RNAi induction, indicating that PATR-1 protein was eliminated from
307 intestinal progenitors by 7 days post RNAi (**Fig. 4J**). Next, control and *patr-1* RNAi
308 intestines were stained for progenitor P-body components EDC3, GE-1 and Me31B.
309 Similar to TRAL, all three of these proteins failed to localize to cytoplasmic foci after
310 *patr-1* RNAi (**Fig. 4K-M**), indicating that the effect we observed with TRAL was a global
311 effect on P-body proteins. Finally, we used SIM to observe localization of EDC3 or
312 TRAL relative to Me31B. Consistent with prior observations, both EDC3 or TRAL
313 colocalized well with Me31B in wildtype intestinal progenitors (**Fig. 4N, P** and quantified
314 in **R, T**). However, this colocalization was lost in the absence of PATR-1 (**Fig. 4O, Q**
315 and quantified in **S, U**), indicating that the overlap of these proteins was dependent
316 upon their localization to P-bodies. Furthermore, compared to wildtype progenitor cells,
317 EDC3, Me31B and TRAL accumulated in much smaller cytoplasmic foci in progenitor
318 cells lacking PATR-1 (compare red and green foci in **Fig. 4N', P'** to **O', Q'**). Taken
319 together, these data indicated that PATR-1 is required for P-body assembly by

320 potentially functioning as a scaffold for these proteins to interact with each other in the
321 cytoplasm of adult *Drosophila* intestinal progenitor cells.
322
323 **Loss of PATR-1 promotes progenitor cell loss**
324 To investigate the role of P-bodies in progenitor cells, we more carefully analyzed
325 the effect of *patr-1* knockdown on progenitor cell biology. To do so, we crossed control
326 and *patr-1* RNAi strains to *esgTS*, and analyzed intestines at three different time points
327 after knock down (1, 7, and 15 days) for an effect on the total number of cells as well as
328 the number of either progenitors, EEs, and ECs (**Fig. 5A**). First, we noted that the
329 intestinal progenitor cell number in *patr-1* RNAi intestines gradually declined over time
330 and was almost completely absent after 15 days of RNAi (**Fig. 5B**). In contrast, EE cell
331 percentage remained unchanged at early time points and showed a slight increase at
332 15 days (**Fig. 5C**). In addition, we observed that the EC percentage increased over time
333 and showed ~30% increase at 15 days (**Fig. 5D**). However, the total number of cells per
334 field was significantly reduced at 15 days (**Fig. 5E**), at least in part reflecting the loss of
335 progenitor cells. Taken together, these data showed that intestinal progenitor cells were
336 lost and the epithelial integrity was compromised by the absence of PATR-1.
337 To verify these RNAi phenotypes, we generated *patr-1* null alleles to
338 independently analyze the consequences of PATR-1 loss in intestinal progenitors.
339 These CRISPR/cas9-induced mutations included four that introduced frameshifts and
340 resulting premature stop codons after the first ~100 amino acids (AAs) of the 968 AA-
341 long protein, as well as four that contained larger ~1kb deletions removing protein-
342 encoding portions of the gene as well as introduced premature stop codons (**Fig. 5F-G**).
343 These new alleles were homozygous lethal, died as third instar larvae, and displayed
344 the same lethal phase when in *trans* to a deficiency. We further verified the absence of
345 PATR-1 protein in mutant third instar larvae by Western blot and, as a positive control,
346 included the *patr-1*^{EY10289} P-element insertion, which inserts UAS sites into the *patr-1*
347 locus and therefore, in conjunction with a ubiquitous Gal4 driver, led to PATR-1
348 overexpression (**Fig. 5H**). We then chose a representative member of each allele type,
349 *patr-1*$^{P105\Delta}$ and *patr-1*^{R107FS1}, to recombine onto an FRT chromosome and analyze in
350 adult progenitors using the Mosaic Analysis with a Repressible Cell Marker (MARCM)

351 technique (Lee and Luo, 1999). Seven days after animals were subjected to clone
352 induction, their intestines were dissected and either stained for PATR-1 or scored for P-
353 body morphology based on Me31B and EDC3 distribution. To rigorously assay for P-
354 body defects, we compared GFP+, HRP+ homozygous mutant progenitor cells with
355 surrounding, heterozygous progenitor cells identified based on HRP staining (compare
356 neighboring ' and " panels in **Fig. 5I-Q**). Consistent with the larval Western blot analysis
357 (**Fig. 5H**), PATR-1 staining was not detected in either *patr-1*$^{P105\Delta}$ or *patr-1*^{R107FS1}
358 homozygous mutant cells (**Fig. 5I-J**). Moreover, a previously verified rescue transgene,
359 *P21M20* (Pradhan et al., 2012), restored the PATR-1 staining in *patr-1*$^{P105\Delta}$
360 homozygous mutant progenitors (**Fig. 5K**). Similar to *patr-1* RNAi, the P-body
361 localization of Me31B and EDC3 was completely disrupted in *patr-1*$^{P105\Delta}$ and *patr-*
362 *1*^{R107FS1} mutant clones (**Fig. 5L-M** and **5O-P**), and these defects were rescued entirely
363 by the *P21M20* transgene (**Fig. 5N** and **5Q**). These data further verified that PATR-1
364 was a necessary component for P-body assembly in adult *Drosophila* intestinal
365 progenitors.
366 We next employed the MARCM technique to induce and track single *patr-1*
367 mutant ISC lineages in heterozygous adults. MARCM clones were analyzed in three
368 ways, all at 7 days after induction. First, the total number of cells per clone was
369 quantified by counting the total number of GFP+ cells per clone. In control intestines,
370 77% of the clones contained greater than 5 cells per clone (**Fig. 5R, V**). By contrast, the
371 two *patr-1* mutants, *patr-1*$^{P105\Delta}$ and *patr-1*^{R107FS1} contained only 45% and 31% clones
372 with greater than 5 cells per clone, respectively (**Fig. 5S, U-V**). Therefore, compared to
373 control, *patr-1* mutant clones contained a smaller number of total cells per clone.
374 Notably, these cell number defects were rescued entirely by the *P21M20* transgene
375 (**Fig. 5T, V**). Second, the number of Delta+ ISCs per clone were counted. Whereas the
376 average number of ISCs per control clone was 1.03±0.92 (n=75), ISC number in *patr-*
377 *1*$^{P105\Delta}$ or *patr-1*^{R107FS1} mutant clones decreased to 0.79±1.16 (n=100) or 0.64±0.77
378 (n=122), respectively (**Fig. 5R-S, U, W**). Compared to 32% of control clones, 53% or
379 48% of *patr-1*$^{P105\Delta}$ or *patr-1*^{R107FS1} mutant clones contained no ISCs (**Fig. 5R-S, U, W**).
380 Furthermore, the average number of ISCs per clone was entirely restored to 1.01±1.02
381 (n=79) by the *P21M20* transgene (**Fig. 5T, W**). Third, we directly quantified the number

382 of PROS+ EE number per clone. Although many clones in all genetic backgrounds
383 lacked EEs, loss of PATR-1 led to a slight reduction in EE-containing clones from 21%
384 in control to 13% or 14% in *patr-1*$^{P105\Delta}$ or *patr-1*^{R107FS1} mutant clones, respectively (**Fig.**
385 **5X**). In combination, both *patr-1* RNAi and *patr-1* loss of function clones suggested that
386 ISCs were lost due to the inability of P-body assembly.
387 To further validate the ISC loss in the absence of PATR-1, we performed one
388 additional experiment. We fed control and flies expressing *patr-1* RNAi (14 days) for 1
389 day with bleomycin, a chemical that induces rapid ISC proliferation due to EC damage
390 and quantified ISC proliferation by staining for phosphorylated-histone 3 (pH3), a highly
391 specific marker for condensed chromosomes (Amcheslavsky et al., 2009). Consistent
392 with ISC loss, we observed significantly low pH3 positive cells in intestines expressing
393 *patr-1* RNAi for 15 days (**Fig. 5Y**). Taken together, *patr-1* RNAi cell number
394 quantification and our detailed clonal analysis showed that ISCs were gradually lost in
395 *patr-1* mutants and the resupply of PATR-1 could reverse these defects.
396
397 **PATR-1 knock-down upregulates pro-differentiation genes in intestinal**
398 **progenitors**
399 To investigate the underlying molecular basis of the progressive loss of
400 progenitor cells caused by the disassembly of P-bodies, we performed transcriptomic
401 profiling (RNA-seq) of FACS (fluorescent activated cell sorting) isolated *patr-1 RNAi* and
402 control intestinal progenitor cells (**Fig. 6A**). Knocking-down *patr-1* in intestinal
403 progenitors significantly altered the expression of 1,226 genes (**Fig. 6B**, **Table S5**). We
404 found that 703 of these genes were significantly upregulated (FDR < 0.05; Log_2 Fold
405 Change > 1) and in contrast 523 genes were significantly downregulated (FDR < 0.05;
406 Log_2 Fold Change < -1) in the absence of PATR-1 (**Fig. 6B-C**, **Table S5**). Importantly
407 we found that, *patr-1* mRNA was the most significantly downregulated gene compared
408 to control, further confirming the efficacy of the RNAi strain we used (**Fig. 6B-D**). We
409 then analyzed this dataset for hallmarks that might explain the loss of progenitor cells.
410 Gene Ontology (GO) analysis of upregulated genes showed significant enrichment of
411 processes including cell differentiation, cell projection morphogenesis, septate junction
412 assembly and cell migration (FDR < 0.05; Fisher's Exact Test). In contrast, GO terms of

413 significantly downregulated genes were associated with biological processes such as
414 biosynthetic processes and certain cell junction assembly processes (FDR < 0.05;
415 Fisher's Exact Test) (**Fig. 6E**, **Table S6**). Although this analysis suggested that ectopic
416 differentiation might be the cause of ISC loss, we also investigated it for other
417 suggestive hallmarks, including inappropriate cell death. To do so, we curated
418 transcriptomic data to assess the expression level of 9 key apoptotic genes: *HtrA2*, *skl*,
419 *Jafrac2*, *rpr*, *hid*, *grim*, *Dronc*, *Drice* and *Dcp-1* (Xu et al., 2009). The transcript level of
420 none of these key cell death effectors was significantly upregulated (**Fig. S3A**, **Table**
421 **S5**), suggesting that the underlying cause of cell loss was independent of apoptotic cell
422 death. Thus, we hypothesized that *patr-1* mutant progenitor cells may have been lost
423 due to elevated differentiation.
424 Consistent with this possibility, we noted that *nub* (*nubbin*, also known as POU-
425 domain protein 1 or *Pdm1*), a key transcription factor that is expressed in ECs and is
426 known to promote their differentiation (Khaminets et al., 2020; Korzelius et al., 2014;
427 Lee et al., 2009), was significantly upregulated in the absence of *patr-1* (**Fig. 6D**, **Table**
428 **S5**). The expression of *nub* in intestinal progenitors is transcriptionally repressed by the
429 Snail family transcription factor, *esg* (*escargot*), which is critical for intestinal progenitor
430 maintenance (Antonello et al., 2015; Khaminets et al., 2020; Korzelius et al., 2014; Li et
431 al., 2017; Loza-Coll et al., 2014). Therefore, the loss of either *esg* itself or of genes that
432 are required for Esg recruitment to target genes, including *vtd* (or *Drosophila* Rad21),
433 promote progenitor cell loss via premature ISC-to-EC differentiation (Khaminets et al.,
434 2020; Korzelius et al., 2014). As with *patr-1*, knockdown of either *esg* or *vtd* also
435 upregulated *nub* expression (Khaminets et al., 2020; Korzelius et al., 2014). To more
436 comprehensively compare the molecular consequences of *patr-1* loss with *esg* and *vtd*
437 loss, we reanalyzed transcriptomic data of *esg* and *vtd* RNAi using an in-house analysis
438 pipeline and cross referenced the significantly upregulated genes in each genetic
439 background to those upregulated after *patr-1* RNAi. We found 22% (92/410 genes) of
440 the significantly upregulated genes in *esg*-RNAi and 18% (80/454 genes) of the
441 significantly upregulated genes in *vtd*-RNAi overlapped with *patr-1* RNAi upregulated
442 genes (**Fig. 6F-G**, **Table S7**). Notably, other EC markers that were upregulated in the
443 *esg* dataset, including *Myo61F* as well as *bbg* (Korzelius et al., 2014), were also

444 upregulated in the *patr-1* dataset (**Fig. 6C, Table S5**). An additional similarity between
445 the *esg* and *patr-1* datasets was the significant upregulation of genes involved in
446 septate junction formation (Korzelius et al., 2014). Septate junction formation is an early
447 step of EC differentiation and its disruption is known to block ISC-EC differentiation
448 (Izumi et al., 2012; Xu et al., 2019). Interestingly, key septate junction genes such as
449 *Tsp2A*, *mesh* and *ssk* (FDR < 0.05; Log_2 Fold Change = 0.84 for PATR-1 RNAi) were
450 noticeably upregulated in both genetic backgrounds (**Fig. S3B**, **Table S5**). However,
451 other septate junction proteins, including *sinu*, *cold, pasi2 and Mcr*, were markedly
452 downregulated in both *patr-1* and *esg* deficient progenitors (**Table S5**). These
453 similarities to *esg* along with GO analysis results of upregulated genes (**Fig. 6E**)
454 suggested that the underlying cause of progenitor loss observed after *patr-1* RNAi could
455 potentially be due to premature ISC-EC differentiation.
456 In addition to these similarities, the *esg* and *patr-1* datasets also displayed some
457 notable differences. For example, while many progenitor cell-specific genes including
458 *mira*, *egfr*, its ligand *spi*, and JAK/STAT receptor *dome* were significantly downregulated
459 in the absence of *esg* (Korzelius et al., 2014), these factors, as well as *esg* itself,
460 showed normal transcript levels in the absence of mature P-bodies (**Fig. 6D**, **S3C**,
461 **Table S5**). In addition, the expression level of *vtd* was unchanged in the absence of
462 PATR-1 (**Fig. S3D**, **Table S5**), suggesting that Esg protein targeting was not
463 compromised by P-body loss. To more comprehensively address whether Esg
464 transcriptional output was disrupted in *patr-1* mutant cells, we evaluated the expression
465 of 76 high confidence *esg* target genes that Korzelius et al., 2014 identified with *esg*
466 DamID and that were highly expressed in *esg* mutant intestinal cells. 24% (18/76) of
467 these were significantly upregulated after *patr-1* knockdown; most were unchanged and
468 approximately 5% (4/76) were significantly downregulated (**Table S7**). Korzelius et al.,
469 2014 also noted that EE marker genes including *prospero* (*pros*), *tachykinin* (*Tk*),
470 *asense* (*ase*) and *Rab3* (Bardin et al., 2010) are upregulated in the absence of *esg*.
471 Interestingly, the transcript level of none of these key factors showed significant
472 changes after *patr-1* loss (**Fig. S3E**, **Table S5**). However, we noted that the expression
473 level of *scute* (*sc*), a well characterized progenitor specific transcription factor (Bardin et
474 al., 2010; Doupé et al., 2018) that promotes EE fate (Li et al., 2017) was significantly

475 upregulated in the absence of PATR-1 (**Fig. S3F**, **Table S5**). Recent studies have
476 shown that both *esg* and *sc* share common binding sites on the *pros* promoter and the
477 binding of one antagonizes the other to alter *pros* expression (Li et al., 2017). Since,
478 *pros* transcript level was not significantly affected in the *patr-1* RNAi background, it was
479 unlikely that the upregulated *sc* drove ISC-to-EE differentiation. Altogether, these
480 observation suggest that PATR-1 promotes progenitor cell maintenance by mediating
481 the post-transcriptional regulation of a subset of *esg* target genes including *nub.*
482 To further evaluate whether *patr-1* loss led to premature ISC-EC differentiation,
483 we compared the transcriptional profiles of *patr-1* deficient intestinal progenitors and
484 ECs using publicly available datasets. We compared significantly upregulated and
485 downregulated genes in *patr-1* RNAi to two different sources. First, we reanalyzed RNA-
486 seq data from FACS-isolated progenitor cells and ECs (Dutta et al., 2015) and
487 performed differential gene expression analysis to identify 478 genes enriched in ECs
488 compared to intestinal progenitors (**Table S8**). Of these enriched genes, 66 genes
489 (14%) genes overlapped with upregulated genes in *patr-1* RNAi (**Fig. S3G**, **Table S8**).
490 In contrast, only 31 (6%) of the 529 genes that were significantly enriched in intestinal
491 progenitors compared to ECs (**Table S8**) overlapped with downregulated genes in *patr-*
492 *1* RNAi (**Fig. S3H**, **Table S8**). Therefore, the *patr-1* RNAi dataset contains more
493 upregulated EC genes than downregulated progenitor genes. Second, we cross-
494 referenced the *patr-1* dataset to a recent cell type specific targeted DamID that
495 identified 965 EC-specific and 1,546 intestinal progenitor-specific protein coding genes
496 (Doupé et al., 2018). Seventy nine (8%) of the EC-specific genes were upregulated in
497 *patr-1* mutant progenitors and, furthermore, 88 (6%) of the progenitor-enriched genes
498 were significantly downregulated in the *patr-1* mutant progenitors (**Fig. 6H-I**, **Table S9**).
499 These data showed that the loss of PATR-1 led to the expression of EC-genes that
500 were ordinarily not expressed in intestinal progenitors. Taken together, data provided
501 here supported a model where P-bodies prevent progenitor differentiation independent
502 of *esg*, and defects in functional P-body assembly could drive progenitor cell loss due to
503 enhanced ISC-EC differentiation.
504
505 **Loss of P-body assembly promotes ISC-EC differentiation**

506 The transcriptomic data of *patr-1* mutant progenitors suggested that enhanced
507 premature ISC-to-EC differentiation was the cause of progenitor cell loss. We performed
508 three additional experiments to experimentally investigate this possibility. First, we
509 quantified the average cell and nuclear area of control and *patr-1* RNAi intestinal
510 progenitors 7 days after RNAi induction, the time point where we observed the onset of
511 cell loss (**Fig. 5B**). Compared to control, both cell and nuclear area of intestinal
512 progenitors were significantly elevated in the absence of PATR-1 (**Fig. 7A-B**). Given
513 that ECs are polyploid and larger than intestinal progenitors, these observations
514 supported the ISC-to-EC differentiation model. Similar results were observed when
515 genes such as *esg* and *vtd*, which are known to promote ISC-to-EC differentiation when
516 knocked down, were eliminated using RNAi (Khaminets et al., 2020; Korzelius et al.,
517 2014). Next, to directly test whether ISC-to-EC differentiation was enhanced, we
518 immunostained control and *patr-1* RNAi intestines for Pdm1 (Khaminets et al., 2020;
519 Korzelius et al., 2014; Lee et al., 2009). Notably, we observed a significant
520 enhancement of GFP+ Pdm1+ cells in intestines lacking *patr-1* (**Fig. 7C-E**). A similar
521 increase in GFP+ Pdm1+ cells were also observed when genes such as *esg*, *vtd*,
522 *Nipped-B* and *polo* were knocked-down (Khaminets et al., 2020; Korzelius et al., 2014).
523 Consistent with transcriptomic data, we observed no increase in GFP+ PROS+ cells,
524 indicating that ISC-to-EE differentiation was not upregulated in the absence of mature
525 P-bodies (**Fig. 7F-G**). Moreover, we experimentally validated that the apoptotic cell
526 death was not enhanced in the absence of PATR-1 (data not shown). Taken together,
527 these observations supported that the cause of progenitor cell loss was enhanced
528 premature ISC-to-EC differentiation. Mechanistically, P-bodies may limit the expression
529 of pro-differentiation genes such as *nub* in intestinal progenitors to maintain the
530 stemness of these cells.
531
532

533 ## Discussion

534 In this study, we characterized a novel population of cytoplasmic mRNPs in
535 *Drosophila* intestinal progenitor cells. We propose these mRNPs are P-bodies based on
536 three main observations: (i) all proteins under investigation are known components of P-
537 bodies in mammalian and yeast cells and show colocalization with each other, (ii) these
538 mRNP granules are significantly larger and show no colocalization with IPSG foci under
539 controlled conditions, and (iii) acute stresses increase the size of these mRNPs and
540 promotes colocalization with IPSGs. Furthermore, our targeted genetic screen identified
541 103 genes that can influence P-body morphology. Of these, we characterized the P-
542 body and cellular effects of *patr-1* loss in intestinal progenitors in detail. PATR-1 is an
543 evolutionary conserved protein with both translational repression and mRNA decay
544 functions (Coller and Parker, 2005; Eulalio et al., 2007a; Scheller et al., 2007; Sheth
545 and Parker, 2003; Teixeira and Parker, 2007). Consistent with its function in
546 *Saccharomyces cerevisiae* (Pilkington and Parker, 2008; Sachdev et al., 2019), this
547 extensive characterization confirmed that PATR-1 is necessary for proper P-body
548 assembly in *Drosophila* intestinal progenitors in a cell-autonomous manner. Loss of P-
549 bodies upregulated the expression of pro-differentiation genes such as *nubbin* and
550 drove premature ISC-to-EC differentiation (**Fig. 8**, right side). Although P-bodies are
551 present in intestinal progenitors, such structures were absent in neighboring
552 differentiated cells. This suggest that P-bodies are disassembled as progenitor cell
553 differentiation proceeds. Collectively, we propose that mature P-bodies are necessary
554 for stem cell maintenance by post-transcriptionally regulating the expression of genes
555 that promote differentiation (**Fig. 8**, left side). Mechanistically, differentiation signals
556 dissolve P-bodies, derepress expression of target differentiation genes, and drive
557 differentiation.

558 As noted previously, a detailed ultrastructural organization of P-bodies at super-
559 resolution has been lacking (Youn et al., 2019). Therefore, we utilized an extensive
560 quantitative super-resolution microscopy-based characterization to show substructures
561 present within mature P-bodies. Consistent with the proposed “core-shell” structure of
562 stress granules (Jain et al., 2016; Niewidok et al., 2018; Wheeler et al., 2016; Youn et
563 al., 2019), P-bodies exhibit “cores” with high protein concentrations and “shells” with low

564 protein concentration (**Fig. 2R-W** and **Fig. 8**). Notably, P-bodies found in intestinal
565 progenitors are considerably smaller than those in mammalian cells such as HEK293
566 cells, with a ~125 nm compared to ~500 nm average diameter (Hubstenberger et al.,
567 2017). Moreover, intestinal progenitors contain ~35-45 mature P-bodies while
568 mammalian cells contain only ~4-7 granules per cell (Hubstenberger et al., 2017). This
569 indicates that the size and the number of mature P-bodies depend on the cell type.
570 The exact molecular function of P-bodies is a matter of current debate (Sachdev
571 et al., 2019). Earlier models proposed that the primary function of P-bodies is mRNA
572 degradation due to the accumulation of mRNA decay factors (Anderson and Kedersha,
573 2006; Decker and Parker, 2012). However, more recent findings propose that P-bodies
574 function as sites of mRNA storage. By sequestering transcripts from translational
575 machinery, P-bodies control the translatome of a cell (Standart and Weil, 2018).
576 Importantly, the transcriptomic approach we took would not be able to identify
577 transcripts that are localized to P-bodies for storage, since no change in the transcript
578 level of such mRNAs would be expected. Other techniques to identify translationally
579 regulated mRNAs, such as polysome profiling, ribosome profiling, RiboTag and
580 translating ribosome affinity purification (TRAP), are not currently feasible in adult
581 *Drosophila* intestinal progenitor cells (Baser et al., 2019; Chassé et al., 2016; Heiman et
582 al., 2014; Ingolia, 2016; King and Gerber, 2014; Tahmasebi et al., 2019). To address
583 this limitation, we are currently developing new tools and techniques to assess changes
584 in translating mRNAs in the presence and absence of mature P-bodies. These new
585 intestinal progenitor profiling techniques will also enable the direct identification of P-
586 body-bound mRNAs using techniques such as enhanced-CLIP (eCLIP) (Van Nostrand
587 et al., 2016) as well as the identification of progenitor-specific microRNAs (Luhur et al.,
588 2013).
589 A recent study documented the presence of P-bodies in cultured embryonic stem
590 cells and suggested their presence in adult stem cells (Di Stefano et al., 2019). In this
591 study, Di Stefano et al. showed that DDX6, the ortholog of *Drosophila* Me31B, mediated
592 P-body assembly and was critical for context-dependent cell fate determination. For
593 example, in some cell types, including endodermally derived progenitors such as Lgr5^{+}
594 ISCs or ectodermally derived progenitors such as neural progenitor cells (NPCs), loss of

595 DDX6 led to a clear expansion of the progenitor cell population, while in other stem cell
596 types, such as mesodermally derived progenitors, loss of DDX6 promoted their
597 differentiation (Di Stefano et al., 2019). Notably, our extensive microscopic
598 characterization and the discovery of P-bodies in *Drosophila* intestinal progenitors verify
599 the presence of mature P-bodies in adult progenitor populations otherwise suggested by
600 Di Stefano et al. However, the loss of P-bodies in *Drosophila* intestinal progenitors
601 promoted the differentiation process (**Fig. 7**) rather than increasing their proliferation, as
602 in Lgr5^{+} ISCs (Di Stefano et al., 2019). There are a few possible explanations that could
603 explain these results. Most simply, it is possible that *Drosophila* intestinal progenitors
604 behave more like mesodermally derived mammalian progenitors rather than endo- or
605 ectodermally derived mammalian progenitors. Alternatively, the stem cell function of
606 DDX6 might be affected by its roles in surrounding cells, since DDX6 was targeted in
607 cells throughout the mouse intestinal organoid whereas PATR-1 was specifically
608 targeted only in progenitor cells in our study. Finally, DDX6-mediated P-body function
609 might be modulated by signaling that might not be fully recapitulated in *in vitro*-derived
610 stem cell models.
611 Consistent with the currently accepted model, P-bodies influence the translation
612 of transcripts encoding fate-instructive transcription and chromatin factors in cultured
613 embryonic and *in vitro*-derived adult stem cells (Di Stefano et al., 2019) . There is also
614 evidence suggesting that P-bodes might affect mRNA stability in stem cells: DDX6
615 together with the mRNA decay factor EDC3 are known to destabilize differentiation-
616 inducing mRNAs such as KLF4 in human epidermal progenitor cells, although it is
617 important to note that P-bodies have not been reported in these cells (Wang et al.,
618 2015). Thus, in adult Drosophila progenitor cells, it is possible that P-body proteins can
619 function to repress translation as well as to degrade certain messages to maintain the
620 behavior of these cells. Interestingly, loss of *patr-1*, which leads to P-body disassembly,
621 significantly upregulated the expression of the EC-fate determinant, *nub*. Therefore, one
622 possibility is that the *nub* mRNA is a P-body-targeted transcript that is subjected to
623 active degradation during stem cell maintenance. If so, differentiation cues that
624 disassemble P-bodies would stabilize the *nub* transcript and its subsequent translation

625 would drive EC differentiation. Despite the appeal of this model, it is still possible that
626 *nub* is transcriptionally upregulated as an indirect effect of P-body disassembly.
627 The transcriptional repression of differentiation genes by the transcription factor
628 *esg* is a key regulatory step of intestinal stem cell maintenance (Antonello et al., 2015;
629 Khaminets et al., 2020; Korzelius et al., 2014; Li et al., 2017; Liu and Jin, 2017; Loza-
630 Coll et al., 2014). For instance, the loss of Esg protein activity promotes ISC-to-EE
631 differentiation through modulation of Notch activity via upregulating Amun, an inhibitor of
632 Notch (Loza-Coll et al., 2014). In contrast, the loss of *esg* gene expression or inability to
633 localize the Esg protein to target genes promote progenitor cell loss via premature ISC-
634 to-EC differentiation (Khaminets et al., 2020; Korzelius et al., 2014). Similar to PATR-1
635 RNAi, knocking down *esg* itself as well as either *vtd*, *Nipped-B* or *polo*, all of which are
636 necessary for recruiting Esg to target promoters, markedly upregulated the expression
637 of Pdm1, the protein product of *nub*, in intestinal progenitors (Khaminets et al., 2020;
638 Korzelius et al., 2014). Notably, our transcriptomic profiling showed that the transcript
639 level of neither *esg* nor any of the Esg-targeting proteins, *vtd*, *Nipped-B* or *polo*, was
640 changed in the absence of mature P-bodies. These observations suggest that Esg
641 protein level and its proper promoter targeting are not affected by the loss of PATR-1.
642 Therefore, we propose that P-bodies post-transcriptionally regulate the expression of
643 EC-fate determinants, independent of Esg-mediated transcriptional regulation. This
644 additional layer of regulation may keep progenitor cells in a primed state where
645 differentiation program can be initiated rapidly and independent of transcription of
646 differentiation genes (Liu et al., 2016; Tahmasebi et al., 2019). This also suggest that
647 the Esg-mediated repression of differentiation genes such as *nub* is not complete and,
648 in anticipation of differentiation, progenitor cells transcribe these genes at basal rates.
649 Our targeted RNAi screen has identified a set of genes that can affect the proper
650 P-body formation in *Drosophila* intestinal progenitor cells. Understanding the
651 mechanisms involved in proper P-body formation is critical for assessing biological
652 functions of these vital cytoplasmic entities (Sachdev et al., 2019). The work presented
653 here showcases the importance of underappreciated post-transcriptional mechanisms
654 to maintain intestinal progenitor function. Future work directed at using recently
655 developed progenitor profiling techniques, such as I-KCKT (Buddika et al., 2020a), to

656 profile mRNA and protein components of progenitor P-bodies will further expand our
657 understanding of P-body function in stem cells within their native tissue contexts.

658 ## Materials and Methods

659

660 ***Drosophila strains and husbandry:***

661 Age matched female flies were used in all experiments. Fly strains were cultured on
662 standard Bloomington *Drosophila* stock center media
663 (https://bdsc.indiana.edu/information/recipes/bloomfood.html) and reared in 18°C, 25°C
664 and 29°C incubators set for a 12hr light/dark schedule and 65% humidity. Flies were
665 cultured in groups of 15-20 (typically 5 males and up to 15 females). All strains used in
666 this study are listed in **Table S1**.

667

668 ***Temperature:***

669 For temporal and regional gene expression-targeting (TARGET) experiments, flies were
670 grown at 18°C, collected over 2 days, and reared in 29°C for up to 20 days before being
671 dissected. For clonal analysis using mosaic analysis with repressible cell marker
672 (MARCM) method, animals were reared at 25°C until eclosion, collected over 2 days
673 and heat-shocked immediately at 37°C for 45 min in a Lauda circulating water bath.
674 Subsequently, flies were reared at 25°C for 7-15 days.

675

676 ***Construction of new strains:***

677 *CRISPR/cas9 mediated generation of Patr-1 alleles*

678 New *Patr-1* alleles were generated by co-injection of two guide RNA (gRNA) plasmids.
679 The gRNA plasmids were generated by subcloning annealed oligos encoding gRNA 5'-
680 catgttgaacatgttatacatgg-3' as well as annealed encoding gRNA 5'-
681 tgtgacgagactgtcggaagggg-3' into the BbsI site of *pU6-BbsI-chiRNA* (Gratz et al 2013).
682 The two resulting plasmids were sequence-verified, amplified, mixed, and co-injected
683 into strain *y^{1} sc* v^{1} sev^{21} ; P{nos-Cas9}attP2* (BL#78782) by Rainbow Genetics
684 (Camarillo CA). Stocks of F_1 progeny were generated, and strains containing new *Patr-*
685 *1* alleles were selected based on non-complementation of the lethality associated with
686 *P{EPgy2}Patr-1^{EY10289}* (BL#19805). New *Patr-1* alleles were molecularly defined by
687 sequencing PCR products generated from genomic DNA obtained from homozygous
688 mutant larvae with oligos flanking the gRNA locations. Two new *Patr-1* alleles as well as

689 *P{EPgy2}Patr-1*^{EY10289} were recombined onto P{FRT}^{82B}-containing chromosomes using
690 standard meiotic methods.
691
692 *UAS-PATR-1 Transgenes*
693 New transgenes were generated by Gibson Assembly using NEBuilder HiFI DNA
694 Assembly Master Mix (New England Biolabs, Catalog E2621), digested plasmids, and
695 PCR products. PCR products containing the PATR-1 open reading frame were
696 amplified from plasmid UFO12408 (Drosophila Genome Resource Center, stock
697 1648643) and combined with homemade attB-plasmids containing either a 3XFLAG or
698 3XFLAG-TEV-GFP cassette. Resulting plasmids were sequence-verified, amplified, and
699 sent to Rainbow Transgenic Flies (Camarillo, CA) for injection into the attP40 site on the
700 second chromosome.
701
702 ***Antibody generation:***
703 Anti-TRAL antibodies were generated in rats (Cocalico Biologicals, Reamstown PA)
704 against a 6XHIS-tagged version of an N-terminal portion of TRAL that was expressed
705 and purified according to standard methods. The TRAL-encoding plasmid was
706 generated by PCR amplifying a 477bp fragment that encodes the first 160 amino acids
707 of TRAL from cDNA GH08269 (DGRC stock 4838) with high-fidelity Q5 polymerase
708 (NEB), subcloning the resulting PCR product into the NcoI and EcoRI sites of
709 pHIS.parallel using HiFi DNA Assembly Master Mix (NEB), and sequence-verifying the
710 resulting plasmid to confirm the absence of any PCR-induced errors.
711
712 Anti-EDC3 antibodies were generated in rabbits and rats (MBL, Japan) against a
713 6XHIS-tagged version of an N-terminal portion of EDC3. The *edc3* coding sequence
714 (corresponding to amino acid 1-440) was PCR-amplified from an ovarian cDNA library
715 using Q5 DNA polymerase (NEB), with primers 5´-
716 GGGAATTCATGGGTCCGACGGATCAAGA-3´ and 5´-
717 GGGGCGGCCGCTCACTTATCGGCACTTATCTCGA-3´. The fragment was digested
718 by *Eco*RI and *Not*I, and cloned into the pProEX HTa vector (Life Technologies). The
719 6×His-tagged Edc3 (1-440) protein was expressed in *E. coli* BL21 cells by IPTG

720 induction, and purified using Ni-NTA agarose resin (Qiagen) under denaturing
721 conditions. The protein was further purified by disc preparative SDS-PAGE using the
722 NA-1800 apparatus (Nihon Eido, Japan). Purified protein fractions were concentrated
723 with Vivaspan-2 (10,000 MWCO PES; Sartorius), dialyzed against PBS containing 4M
724 urea followed by PBS/2M urea. Polyclonal antibodies were affinity-purified with the
725 same antigen immobilized on HiTrap NHS columns (GE Healthcare).
726
727 ***Dissections and immunostaining:***
728 Gastrointestinal (GI) tracts of adult female flies were dissected in ice-cold 1xPBS and
729 fixed in 4% paraformaldehyde (Electron Microscopy Sciences, Cat. No. 15714) in PBS
730 for 45 min. These samples were washed with 1xPBT (1xPBS, 0.1% Triton X-100) and
731 then blocked (1xPBT, 0.5% Bovine Serum Albumin) for at least 45 min. Subsequently,
732 samples were incubated at 4°C overnight with primary antibodies, including rabbit anti-
733 GFP (A11122, Life Technologies, 1:1000), mouse anti-V5 (MCA1360GA, Bio-Rad,
734 1:250), mouse anti-FLAG (F3165, Sigma, 1:1000), rabbit anti-HA (3724S, Cell Signaling
735 Technology, 1:1000), mouse anti-FMR1 (5A11, Developmental Studies Hybridoma
736 Bank, 1:100), mouse anti-Prospero (MR1A, Developmental Studies Hybridoma Bank,
737 1:100), mouse anti-Delta (C594.9B, Developmental Studies Hybridoma Bank, 1:500),
738 rat anti-TRAL (this study, 1:1500), rabbit anti-Me31B (Nakamura A, Amikura R, Hanyu
739 K, 2001) (1:2000), mouse anti-Me31B (Barbee et al., 2006) (1:1500), rabbit anti-Ge-1
740 (Fan et al., 2011) (1:500), rat anti-EDC3 (this study, 1:1500), rabbit anti-EDC3 (this
741 study, 1:2000) and rabbit anti-Pdm1 (a gift from Xiaohang Yang) (1:1500). Samples
742 were washed and incubated for 2-3 hours with secondary antibodies, including
743 AlexaFluor-488 and -568-conjugated goat anti-rabbit, -mouse and -rat antibodies (Life
744 Technologies, 1:1000). AlexaFluor-647 conjugated goat-HRP antibodies were used in
745 the secondary antibody solution whenever required. Samples were washed and treated
746 with DAPI (1:10000) and mounted in Vectashield (Vecta Laboratories). An alternative
747 staining protocol was used for Delta staining as described in Buddika et al., 2020a.
748
749 ***Microscopy and image processing:***

750 Images were collected on either a Leica SP8 Scanning Confocal microscope (Leica
751 DMi8 inverted microscope platform; equipped with WLL 470-670 nm, 405 nm and 440
752 nm lasers, Huygens deconvolution software; controlled by Leica LAS-X software; image
753 acquisition using Leica HC PL APO CS2 63x/1.40 or Leica HC PL APO CS2 40x/1.40
754 lens with Leica Type F Immersion Liquid (N = 1.518)) or an OMX 3D-SIM Super-
755 Resolution microscope (DeltaVision OMX system; equipped with 405, 488, 561, 642 nm
756 lasers; controlled by AquireSR software; image processing by SoftWorx imaging
757 software; image acquisition using an Olympus PL APO N 60x/1.42 lens with Applied
758 Precision Immersion Oil (N = 1.518)) available at the Light Microscopy Imaging Center,
759 Indiana University, Bloomington. Whenever possible, samples to be compared were
760 collected under identical settings on the same day, image files were adjusted
761 simultaneously using Adobe Photoshop CC, and figures were assembled using Adobe
762 Illustrator CC. ImageJ FIJI (https://fiji.sc/) Analyze Particles plugin was used to quantify
763 the average area of granules using 0.01μm^2 as the lower cut off of puncta size. The
764 ImageJ FIJI Plot Profile plugin was used to generate line plots.
765
766 ***Ex-vivo treatments:***
767 All *ex-vivo* treatments were performed as described in Buddika et al., JCS, 2020.
768 Briefly, intestines from females aged 8-10 days on normal diet were incubated in Krebs-
769 Ringer media/KRB (Alfa Aesar, Cat. No. J67591) or KRB supplemented with 1mM
770 rapamycin (LC Laboratories, Cat. No. r-5000) for 60 min and then fixed.
771
772 ***Protein isolation and western blot analysis:***
773 Wandering L3 larvae or adult female flies were used for protein isolation. Collected
774 larvae or adult flies were lysed in I-RIPA protein lysis buffer (150mM NaCl, 50mM Tris-
775 HCl pH 7.5, 1mM EDTA, 1% Triton X-100, 1% Na Deoxycholic Acid, 1xprotease
776 inhibitor cocktail), protein extracts were resolved on a 4-20% gradient polyacrylamide
777 gel (Bio-Rad, Cat. No. 456-1093), transferred to Immobilon®-P membrane (Millipore,
778 Cat. No. IPVH00010) and probed with rat anti-TRAL (1:2000, this study), rat anti-PATR1
779 (Pradhan et al., 2012) (1:2000) or mouse anti-a-tubulin (12G10, Developmental Studies
780 Hybridoma Bank, 1:1000) antibodies. Subsequently, blots were washed extensively with

781 1xTBST (1xTBS, 0.1% Tween-20) and incubated with anti-rat or -mouse conjugated
782 HRP secondary antibodies. After extensive secondary washes with 1xTBST, blots were
783 treated with ECL-detection reagent 1 and 2 (Thermo Scientific, Cat. No. 1859701 and
784 1859698) and finally exposed to chemiluminescence films (GE Healthcare, Cat. No.
785 28906839) and developed the signal.
786
787 ***FACS isolation of progenitor cells and RNA-seq library preparation:***
788 Gastrointestinal (GI) tracts of 100 adult female flies (per replicate) were dissected in ice-
789 cold 1xPBS. Then cells were dissociated by treating intestines with 1mg/ml elastase at
790 27°C for 1 hour with agitation. Subsequently, ~30,000-50,000 GFP^{+} intestinal progenitor
791 cells were sorted using a BD FACSAria^{TM} II flow cytometer equipped with a 100µm
792 nozzle at the IUB Flow Cytometry Core Facility. Total RNA was prepared using the
793 TRIzol® LS reagent (cat.no.) and rRNA-depleted libraries were prepared using the
794 Ovation® SoLo RNA-seq system (Part No. 0502 including Parts 0407 and S02240)
795 following manufacturer's instructions. The quality and quantity of final libraries were
796 assessed using Agilent 2200 TapeStation and KAPA Library Quantification Kit,
797 respectively.
798
799 ***RNA-seq data analysis:***
800 Transcriptomic data analysis was performed as described in Buddika et al., 2020a using
801 a python based in-house pipeline (https://github.com/jkkbuddika/RNA-Seq-Data-
802 Analyzer). Briefly, the quality of raw sequencing files was assessed using FastQC
803 (Andrews, 2010) version 0.11.9, low quality reads were eliminated using Cutadapt
804 (Martin, 2011) version 2.9, and reads mapping to rRNAs were removed using TagDust2
805 (Lassmann, 2015) version 2.2. Next, the remaining reads were mapped to the Berkeley
806 *Drosophila* Genome Project (BDGP) assembly release 6.28 (Ensembl release 100)
807 reference genome using STAR genome aligner (Dobin et al., 2013) version 2.7.3a and
808 duplicated reads were removed using SAMtools (Li et al., 2009) version 1.10.
809 Subsequently, the Subread (Liao et al., 2019) version 2.0.0 function *featureCounts* was
810 used to count the number of aligned reads to the nearest overlapping feature. Finally,
811 bigWig files representing RNA-seq coverage were generated using deepTools (Ramírez

et al., 2016) version 3.4.2 with the settings --normalizeUsing CPM --binSize 1. Differential gene expression analysis was performed with the Bioconductor package DESeq2 (https://bioconductor.org/packages/release/bioc/html/DESeq2.html) (Love et al., 2014) version 1.26.0. Unless otherwise noted, significantly upregulated and downregulated genes were defined as FDR < 0.05; Log_2 fold change > 1 and FDR < 0.05; Log_2 fold change < -1, respectively and were used to identify enriched Gene Ontology (GO) terms using PANTHER overrepresentation analysis on GO Consortium (http://geneontology.org/). A selected significantly enriched GO categories were plotted. All data visualization steps were performed using custom scripts written using R.

Statistical analysis:

GraphPad Prism, Version 7.0 was used for all statistical analyses. First, the normality of datasets was tested using D'Agostino-Pearson test. For comparisons involved in two datasets, if datasets follow [1] a parametric distribution, an Unpaired t-test or [2] a non-parametric distribution, a Mann-Whitney test was performed. Three or more datasets following a parametric distribution were analyzed using an ordinary one-way ANOVA test. Multiple comparisons of three or more datasets following a non-parametric distribution were analyzed using Kruskal-Wallis test. Unless otherwise noted, significance is indicated as follows: n.s., not significant; *p < 0.05; **p < 0.01; ***p < 0.001; ****p < 0.0001.

Acknowledgements

We thank Scott Barbee, Anne Ephrussi, Xiaohang Yang, the Bloomington *Drosophila* Stock Center (supported by grant NIHP4OOD018537), the *Drosophila* Genome Resource Center (supported by grant NIH2P40OD010949), and the Developmental Studies Hybridoma Bank (created by the NICHD of the NIH) for reagents; Robert Policastro for bioinformatics expertise; the Light Microscopy Imaging Center (supported by grant NIH1S10OD024988-01) for access to the SP8 confocal and OMX super-resolution microscopes; the Flow Cytometry Core Facility at Indiana University, Bloomington for access to the BD FACSAria™ II flow cytometer.

Competing Interests

The authors declare no competing financial interests.

Funding

This work was supported by the National Institute of General Medical Sciences (Award R01GM124220).

853 ## References

854 **Amcheslavsky, A., Jiang, J. and Ip, Y. T.** (2009). Tissue damage-induced intestinal
855 stem cell division in Drosophila. *Cell Stem Cell* **4**, 49–61.

856 **Anderson, P. and Kedersha, N.** (2006). RNA granules. *J. Cell Biol.* **172**, 803–808.

857 **Anderson, P. and Kedersha, N.** (2009). Stress granules. *Curr. Biol.* **19**, R397-8.

858 **Anderson, E. N., Gochenaur, L., Singh, A., Grant, R., Patel, K., Watkins, S., Wu, J.**
859 **Y. and Pandey, U. B.** (2018). Traumatic injury induces stress granule formation
860 and enhances motor dysfunctions in ALS/FTD models. *Hum. Mol. Genet.* **27**,
861 1366–1381.

862 **Andrews, S.** (2010). FastQC: A quality control tool for high throughput sequence data.

863 **Antonello, Z. A., Reiff, T., Ballesta-Illan, E. and Dominguez, M.** (2015). Robust
864 intestinal homeostasis relies on cellular plasticity in enteroblasts mediated by miR-
865 8–Escargot switch. *EMBO J.* **34**, 2025–2041.

866 **Ayache, J., Bénard, M., Ernoult-Lange, M., Minshall, N., Standart, N., Kress, M. and**
867 **Weil, D.** (2015). P-body assembly requires DDX6 repression complexes rather than
868 decay or Ataxin2/2L complexes. *Mol. Biol. Cell* **26**, 2579–95.

869 **Barbee, S. A., Estes, P. S., Cziko, A.-M., Hillebrand, J., Luedeman, R. A., Coller, J.**
870 **M., Johnson, N., Howlett, I. C., Geng, C., Ueda, R., et al.** (2006). Staufen- and
871 FMRP-containing neuronal RNPs are structurally and functionally related to
872 somatic P bodies. *Neuron* **52**, 997–1009.

873 **Bardin, A. J., Perdigoto, C. N., Southall, T. D., Brand, A. H. and Schweisguth, F.**
874 (2010). Transcriptional control of stem cell maintenance in the Drosophila intestine.
875 *Development* **137**, 705–14.

876 **Baser, A., Skabkin, M., Kleber, S., Dang, Y., Gülcüler Balta, G. S., Kalamakis, G.,**
877 **Göpferich, M., Ibañez, D. C., Schefzik, R., Lopez, A. S., et al.** (2019). Onset of
878 differentiation is post-transcriptionally controlled in adult neural stem cells. *Nature*
879 **566**, 100–104.

880 **Bashkirov, V. I., Scherthan, H., Solinger, J. A., Buerstedde, J.-M. and Heyer, W.-D.**
881 (1997). A Mouse Cytoplasmic Exoribonuclease (mXRN1p) with Preference for G4
882 Tetraplex Substrates. *J. Cell Biol.* **136**, 761–773.

883 **Batista, P. J., Molinie, B., Wang, J., Qu, K., Zhang, J., Li, L., Bouley, D. M., Lujan,**

884 **E., Haddad, B., Daneshvar, K., et al.** (2014). m6A RNA Modification Controls Cell
885 Fate Transition in Mammalian Embryonic Stem Cells. *Cell Stem Cell* **15**, 707–719.
886 **Bertero, A., Brown, S., Madrigal, P., Osnato, A., Ortmann, D., Yiangou, L.,**
887 **Kadiwala, J., Hubner, N. C., de los Mozos, I. R., Sadée, C., et al.** (2018). The
888 SMAD2/3 interactome reveals that TGFβ controls m6A mRNA methylation in
889 pluripotency. *Nature* **555**, 256–259.
890 **Bhattacharyya, S. N., Habermacher, R., Martine, U., Closs, E. I. and Filipowicz, W.**
891 (2006). Relief of microRNA-Mediated Translational Repression in Human Cells
892 Subjected to Stress. *Cell* **125**, 1111–1124.
893 **Brengues, M., Teixeira, D. and Parker, R.** (2005). Decapping and Decay of
894 Messenger RNA Occur in Cytoplasmic Processing Bodies. *Science (80-.).* **300**,
895 805–808.
896 **Brumbaugh, J., Stefano, B. Di, Wang, X., Borkent, M., Forouzmand, E., Clowers, K.**
897 **J., Ji, F., Schwarz, B. A., Kalocsay, M., Elledge, S. J., et al.** (2018). Nudt21
898 Controls Cell Fate by Connecting Alternative Polyadenylation to Chromatin
899 Signaling. *Cell* **172**, 106-120.e21.
900 **Buchan, J. R. and Parker, R.** (2009). Eukaryotic Stress Granules: The Ins and Outs of
901 Translation. *Mol. Cell* **36**, 932–941.
902 **Buddika, K., Xu, J., Ariyapala, I. S. and Sokol, N. S.** (2020a). I-KCKT allows
903 dissection-free RNA profiling of adult Drosophila intestinal progenitor cells. *bioRxiv*.
904 **Buddika, K., Ariyapala, I. S., Hazuga, M. A., Riffert, D. and Sokol, N. S.** (2020b).
905 Canonical nucleators are dispensable for stress granule assembly in Drosophila
906 intestinal progenitors. *J. Cell Sci.* **133**,.
907 **Chan, L. Y., Mugler, C. F., Heinrich, S., Vallotton, P. and Weis, K.** (2018). Non-
908 invasive measurement of mRNA decay reveals translation initiation as the major
909 determinant of mRNA stability. *Elife* **7**,.
910 **Chassé, H., Boulben, S., Costache, V., Cormier, P. and Morales, J.** (2016). Analysis
911 of translation using polysome profiling. *Nucleic Acids Res.* **45**, gkw907.
912 **Chen, C.-H., Luhur, A. and Sokol, N.** (2015). Lin-28 promotes symmetric stem cell
913 division and drives adaptive growth in the adult Drosophila intestine. *Development*
914 **142**, 3478–87.

915 **Coller, J. and Parker, R.** (2005). General translational repression by activators of
916 mRNA decapping. *Cell* **122**, 875–86.
917 **Conway, A. E., Van Nostrand, E. L., Pratt, G. A., Aigner, S., Wilbert, M. L.,**
918 **Sundararaman, B., Freese, P., Lambert, N. J., Sathe, S., Liang, T. Y., et al.**
919 (2016). Enhanced CLIP Uncovers IMP Protein-RNA Targets in Human Pluripotent
920 Stem Cells Important for Cell Adhesion and Survival. *Cell Rep.* **15**, 666–679.
921 **Decker, C. J. and Parker, R.** (2012). P-Bodies and Stress Granules: Possible Roles in
922 the Control of Translation and mRNA Degradation. *Cold Spring Harb. Perspect.*
923 *Biol.* **4**, a012286.
924 **Di Stefano, B., Luo, E.-C., Haggerty, C., Aigner, S., Charlton, J., Brumbaugh, J., Ji,**
925 **F., Rabano Jiménez, I., Clowers, K. J., Huebner, A. J., et al.** (2019). The RNA
926 Helicase DDX6 Controls Cellular Plasticity by Modulating P-Body Homeostasis.
927 *Cell Stem Cell* **25**, 622-638.e13.
928 **Dijk, E. van, Hir, H. Le and Séraphin, B.** (2003). DcpS can act in the 5′–3′ mRNA
929 decay pathway in addition to the 3′–5′ pathway. *Proc. Natl. Acad. Sci.* **100**, 12081–
930 12086.
931 **Dobin, A., Davis, C. A., Schlesinger, F., Drenkow, J., Zaleski, C., Jha, S., Batut, P.,**
932 **Chaisson, M. and Gingeras, T. R.** (2013). STAR: ultrafast universal RNA-seq
933 aligner. *Bioinformatics* **29**, 15–21.
934 **Doupé, D. P., Marshall, O. J., Dayton, H., Brand, A. H. and Perrimon, N.** (2018).
935 Drosophila intestinal stem and progenitor cells are major sources and regulators of
936 homeostatic niche signals. *Proc. Natl. Acad. Sci. U. S. A.* **115**, 12218–12223.
937 **Dutta, D., Dobson, A. J., Houtz, P. L., Gläßer, C., Revah, J., Korzelius, J., Patel, P.**
938 **H., Edgar, B. A. and Buchon, N.** (2015). Regional Cell-Specific Transcriptome
939 Mapping Reveals Regulatory Complexity in the Adult Drosophila Midgut. *Cell Rep.*
940 **12**, 346–358.
941 **Eulalio, A., Behm-Ansmant, I. and Izaurralde, E.** (2007a). P bodies: at the crossroads
942 of post-transcriptional pathways. *Nat. Rev. Mol. Cell Biol.* **8**, 9–22.
943 **Eulalio, A., Behm-Ansmant, I., Schweizer, D. and Izaurralde, E.** (2007b). P-body
944 formation is a consequence, not the cause, of RNA-mediated gene silencing. *Mol.*
945 *Cell. Biol.* **27**, 3970–81.

946 **Eystathioy, T., Jakymiw, A., Chan, E. K. L., Seraphin, B., Cougot, N. and Fritzler,**
947 **M. J.** (2003). The GW182 protein colocalizes with mRNA degradation associated
948 proteins hDcp1 and hLSm4 in cytoplasmic GW bodies. *RNA* **9**, 1171–1173.
949 **Fan, S.-J., Marchand, V. and Ephrussi, A.** (2011). Drosophila Ge-1 Promotes P Body
950 Formation and oskar mRNA Localization. *PLoS One* **6**, e20612.
951 **Franks, T. M. and Lykke-Andersen, J.** (2008). The Control of mRNA Decapping and
952 P-Body Formation. *Mol. Cell* **32**, 605–615.
953 **Gareau, C., Houssin, E., Martel, D., Coudert, L., Mellaoui, S., Huot, M.-E., Laprise,**
954 **P. and Mazroui, R.** (2013). Characterization of Fragile X Mental Retardation
955 Protein Recruitment and Dynamics in Drosophila Stress Granules. *PLoS One* **8**,
956 e55342.
957 **Guallar, D., Bi, X., Pardavila, J. A., Huang, X., Saenz, C., Shi, X., Zhou, H., Faiola,**
958 **F., Ding, J., Haruehanroengra, P., et al.** (2018). RNA-dependent chromatin
959 targeting of TET2 for endogenous retrovirus control in pluripotent stem cells. *Nat.*
960 *Genet.* **50**, 443–451.
961 **Han, H., Irimia, M., Ross, P. J., Sung, H.-K., Alipanahi, B., David, L., Golipour, A.,**
962 **Gabut, M., Michael, I. P., Nachman, E. N., et al.** (2013). MBNL proteins repress
963 ES-cell-specific alternative splicing and reprogramming. *Nature* **498**, 241–245.
964 **Heiman, M., Kulicke, R., Fenster, R. J., Greengard, P. and Heintz, N.** (2014). Cell
965 type–specific mRNA purification by translating ribosome affinity purification (TRAP).
966 *Nat. Protoc.* **9**, 1282–1291.
967 **Hubstenberger, A., Courel, M., Bénard, M., Souquere, S., Ernoult-Lange, M.,**
968 **Chouaib, R., Yi, Z., Morlot, J.-B., Munier, A., Fradet, M., et al.** (2017). P-Body
969 Purification Reveals the Condensation of Repressed mRNA Regulons. *Mol. Cell*
970 **68**, 144-157.e5.
971 **Ingelfinger, D., Arndt-Jovin, D. J., Lührmann, R. and Achsel, T.** (2002). The human
972 LSm1-7 proteins colocalize with the mRNA-degrading enzymes Dcp1/2 and Xrnl in
973 distinct cytoplasmic foci. *RNA* **8**, 1489–1501.
974 **Ingolia, N. T.** (2016). Ribosome Footprint Profiling of Translation throughout the
975 Genome. *Cell* **165**, 22–33.
976 **Izumi, Y., Yanagihashi, Y. and Furuse, M.** (2012). A novel protein complex, Mesh-

977 Ssk, is required for septate junction formation in the Drosophila midgut. *J. Cell Sci.*
978 **125**, 4923–33.
979 **Jain, S., Wheeler, J. R., Walters, R. W., Agrawal, A., Barsic, A. and Parker, R.**
980 (2016). ATPase-Modulated Stress Granules Contain a Diverse Proteome and
981 Substructure. *Cell* **164**, 487–498.
982 **Jevtov, I., Zacharogianni, M., van Oorschot, M. M., van Zadelhoff, G., Aguilera-**
983 **Gomez, A., Vuillez, I., Braakman, I., Hafen, E., Stocker, H. and Rabouille, C.**
984 (2015). TORC2 mediates the heat stress response in Drosophila by promoting the
985 formation of stress granules. *J. Cell Sci.* **128**, 2497–508.
986 **Kedersha, N., Cho, M. R., Li, W., Yacono, P. W., Chen, S., Gilks, N., Golan, D. E.**
987 **and Anderson, P.** (2000). Dynamic Shuttling of Tia-1 Accompanies the
988 Recruitment of mRNA to Mammalian Stress Granules. *J. Cell Biol.* **151**, 1257–
989 1268.
990 **Kedersha, N., Stoecklin, G., Ayodele, M., Yacono, P., Lykke-Andersen, J., Fritzler,**
991 **M. J., Scheuner, D., Kaufman, R. J., Golan, D. E. and Anderson, P.** (2005).
992 Stress granules and processing bodies are dynamically linked sites of mRNP
993 remodeling. *J. Cell Biol.* **169**, 871–884.
994 **Khaminets, A., Ronnen-Oron, T., Baldauf, M., Meier, E. and Jasper, H.** (2020).
995 Cohesin controls intestinal stem cell identity by maintaining association of Escargot
996 with target promoters. *Elife* **9**,.
997 **King, H. A. and Gerber, A. P.** (2014). Translatome profiling: methods for genome-scale
998 analysis of mRNA translation. *Brief. Funct. Genomics* **15**, 22–31.
999 **Korzelius, J., Naumann, S. K., Loza-Coll, M. A., Chan, J. S., Dutta, D., Oberheim,**
1000 **J., Gläßer, C., Southall, T. D., Brand, A. H., Jones, D. L., et al.** (2014). *Escargot*
1001 maintains stemness and suppresses differentiation in *Drosophila* intestinal stem
1002 cells. *EMBO J.* **33**, 2967–2982.
1003 **Lackford, B., Yao, C., Charles, G. M., Weng, L., Zheng, X., Choi, E.-A., Xie, X., Wan,**
1004 **J., Xing, Y., Freudenberg, J. M., et al.** (2014). Fip1 regulates mRNA alternative
1005 polyadenylation to promote stem cell self-renewal. *EMBO J.* **33**, 878–889.
1006 **Lassmann, T.** (2015). TagDust2: a generic method to extract reads from sequencing
1007 data. *BMC Bioinformatics* **16**, 24.

1008 **Lee, T. and Luo, L.** (1999). Mosaic Analysis with a Repressible Cell Marker for Studies
1009 of Gene Function in Neuronal Morphogenesis. *Neuron* **22**, 451–461.
1010 **Lee, W.-C., Beebe, K., Sudmeier, L. and Micchelli, C. A.** (2009). Adenomatous
1011 polyposis coli regulates Drosophila intestinal stem cell proliferation. *Development*
1012 **136**, 2255–64.
1013 **Li, H., Handsaker, B., Wysoker, A., Fennell, T., Ruan, J., Homer, N., Marth, G.,**
1014 **Abecasis, G., Durbin, R. and 1000 Genome Project Data Processing Subgroup**
1015 (2009). The Sequence Alignment/Map format and SAMtools. *Bioinformatics* **25**,
1016 2078–9.
1017 **Li, Y., Pang, Z., Huang, H., Wang, C., Cai, T. and Xi, R.** (2017). Transcription Factor
1018 Antagonism Controls Enteroendocrine Cell Specification from Intestinal Stem Cells.
1019 *Sci. Rep.* **7**, 988.
1020 **Liao, Y., Smyth, G. K. and Shi, W.** (2019). The R package Rsubread is easier, faster,
1021 cheaper and better for alignment and quantification of RNA sequencing reads.
1022 *Nucleic Acids Res.* **47**, e47.
1023 **Liu, Q. and Jin, L. H.** (2017). Tissue-resident stem cell activity: a view from the adult
1024 Drosophila gastrointestinal tract. *Cell Commun. Signal.* **15**, 33.
1025 **Liu, Y., Beyer, A. and Aebersold, R.** (2016). On the Dependency of Cellular Protein
1026 Levels on mRNA Abundance. *Cell* **165**, 535–50.
1027 **Love, M. I., Huber, W. and Anders, S.** (2014). Moderated estimation of fold change
1028 and dispersion for RNA-seq data with DESeq2. *Genome Biol.* **15**, 550.
1029 **Loza-Coll, M. A., Southall, T. D., Sandall, S. L., Brand, A. H. and Jones, D. L.**
1030 (2014). Regulation of Drosophila intestinal stem cell maintenance and
1031 differentiation by the transcription factor Escargot. *EMBO J.* **33**, 2983–96.
1032 **Lu, X., Göke, J., Sachs, F., Jacques, P.-É., Liang, H., Feng, B., Bourque, G.,**
1033 **Bubulya, P. A. and Ng, H.-H.** (2013). SON connects the splicing-regulatory
1034 network with pluripotency in human embryonic stem cells. *Nat. Cell Biol.* **15**, 1141–
1035 1152.
1036 **Luhur, A., Chawla, G. and Sokol, N. S.** (2013). MicroRNAs as Components of
1037 Systemic Signaling Pathways in Drosophila melanogaster. *Curr. Top. Dev. Biol.*
1038 **105**, 97–123.

1039 **Luhur, A., Buddika, K., Ariyapala, I. S., Chen, S. and Sokol, N. S.** (2017). Opposing
1040 Post-transcriptional Control of InR by FMRP and LIN-28 Adjusts Stem Cell-Based
1041 Tissue Growth. *Cell Rep.* **21**, 2671–2677.
1042 **Luo, Y., Na, Z. and Slavoff, S. A.** (2018). P-Bodies: Composition, Properties, and
1043 Functions. *Biochemistry* **57**, 2424–2431.
1044 **Martin, M.** (2011). Cutadapt removes adapter sequences from high-throughput
1045 sequencing reads. *EMBnet.journal* **17**, 10.
1046 **Martínez, J. P., Pérez-Vilaró, G., Muthukumar, Y., Scheller, N., Hirsch, T., Diestel,**
1047 **R., Steinmetz, H., Jansen, R., Frank, R., Sasse, F., et al.** (2013). Screening of
1048 small molecules affecting mammalian P-body assembly uncovers links with diverse
1049 intracellular processes and organelle physiology. *RNA Biol.* **10**, 1661–9.
1050 **Micchelli, C. A. and Perrimon, N.** (2006). Evidence that stem cells reside in the adult
1051 Drosophila midgut epithelium. *Nature* **439**, 475–479.
1052 **Mugler, C. F., Hondele, M., Heinrich, S., Sachdev, R., Vallotton, P., Koek, A. Y.,**
1053 **Chan, L. Y. and Weis, K.** (2016). ATPase activity of the DEAD-box protein Dhh1
1054 controls processing body formation. *Elife* **5**,.
1055 **Nakamura A, Amikura R, Hanyu K, K. S.** (2001). Me31B silences translation of
1056 oocyte-localizing RNAs through the formation of cytoplasmic RNP complex during
1057 Drosophila oogenesis. *Development* **128**, 3233–3242.
1058 **Niewidok, B., Igaev, M., Pereira da Graca, A., Strassner, A., Lenzen, C., Richter, C.**
1059 **P., Piehler, J., Kurre, R. and Brandt, R.** (2018). Single-molecule imaging reveals
1060 dynamic biphasic partition of RNA-binding proteins in stress granules. *J. Cell Biol.*
1061 **217**, 1303–1318.
1062 **Nissan, T., Rajyaguru, P., She, M., Song, H. and Parker, R.** (2010). Decapping
1063 activators in Saccharomyces cerevisiae act by multiple mechanisms. *Mol. Cell* **39**,
1064 773–83.
1065 **O'Brien, L. E., Soliman, S. S., Li, X. and Bilder, D.** (2011). Altered Modes of Stem
1066 Cell Division Drive Adaptive Intestinal Growth. *Cell* **147**, 603–614.
1067 **Ohlstein, B. and Spradling, A.** (2006). The adult Drosophila posterior midgut is
1068 maintained by pluripotent stem cells. *Nature* **439**, 470–474.
1069 **Parker, R. and Sheth, U.** (2007). P Bodies and the Control of mRNA Translation and

1070 Degradation. *Mol. Cell* **25**, 635–646.
1071 **Pilkington, G. R. and Parker, R.** (2008). Pat1 contains distinct functional domains that
1072 promote P-body assembly and activation of decapping. *Mol. Cell. Biol.* **28**, 1298–
1073 312.
1074 **Pradhan, S. J., Nesler, K. R., Rosen, S. F., Kato, Y., Nakamura, A., Ramaswami, M.**
1075 **and Barbee, S. A.** (2012). The conserved P body component HPat/Pat1 negatively
1076 regulates synaptic terminal growth at the larval Drosophila neuromuscular junction.
1077 *J. Cell Sci.* **125**, 6105–16.
1078 **Protter, D. S. W. and Parker, R.** (2016). Principles and Properties of Stress Granules.
1079 *Trends Cell Biol.* **26**, 668–679.
1080 **Ramírez, F., Ryan, D. P., Grüning, B., Bhardwaj, V., Kilpert, F., Richter, A. S.,**
1081 **Heyne, S., Dündar, F. and Manke, T.** (2016). deepTools2: a next generation web
1082 server for deep-sequencing data analysis. *Nucleic Acids Res.* **44**, W160–W165.
1083 **Sachdev, R., Hondele, M., Linsenmeier, M., Vallotton, P., Mugler, C. F., Arosio, P.**
1084 **and Weis, K.** (2019). Pat1 promotes processing body assembly by enhancing the
1085 phase separation of the DEAD-box ATPase Dhh1 and RNA. *Elife* **8**,.
1086 **Scheller, N., Resa-Infante, P., de la Luna, S., Galao, R. P., Albrecht, M., Kaestner,**
1087 **L., Lipp, P., Lengauer, T., Meyerhans, A. and Díez, J.** (2007). Identification of
1088 PatL1, a human homolog to yeast P body component Pat1. *Biochim. Biophys. Acta*
1089 *- Mol. Cell Res.* **1773**, 1786–1792.
1090 **Sheth, U. and Parker, R.** (2003). Decapping and Decay of Messenger RNA Occur in
1091 Cytoplasmic Processing Bodies. *Science (80-.).* **300**, 805–808.
1092 **Standart, N. and Weil, D.** (2018). P-Bodies: Cytosolic Droplets for Coordinated mRNA
1093 Storage. *Trends Genet.* **34**, 612–626.
1094 **Stoecklin, G., Mayo, T. and Anderson, P.** (2006). ARE-mRNA degradation requires
1095 the 5′–3′ decay pathway. *EMBO Rep.* **7**, 72–77.
1096 **Tahmasebi, S., Amiri, M. and Sonenberg, N.** (2019). Translational Control in Stem
1097 Cells. *Front. Genet.* **9**, 709.
1098 **Teixeira, D. and Parker, R.** (2007). Analysis of P-Body Assembly in *Saccharomyces*
1099 *cerevisiae*. *Mol. Biol. Cell* **18**, 2274–2287.
1100 **Teixeira, D., Sheth, U., Valencia-Sanchez, M. A., Brengues, M. and Parker, R.**

1101 (2005). Processing bodies require RNA for assembly and contain nontranslating
1102 mRNAs. *RNA* **11**, 371–382.
1103 **V, R., KH, S. and PK, H.** (2011). The cAMP-dependent Protein Kinase Signaling
1104 Pathway Is a Key Regulator of P Body Foci Formation. *Mol. Cell* **43**,.
1105 **van Dijk, E., Cougot, N., Meyer, S., Babajko, S., Wahle, E. and Séraphin, B.** (2002).
1106 Human Dcp2: a catalytically active mRNA decapping enzyme located in specific
1107 cytoplasmic structures. *EMBO J.* **21**, 6915–6924.
1108 **Van Nostrand, E. L., Pratt, G. A., Shishkin, A. A., Gelboin-Burkhart, C., Fang, M. Y.,**
1109 **Sundararaman, B., Blue, S. M., Nguyen, T. B., Surka, C., Elkins, K., et al.**
1110 (2016). Robust transcriptome-wide discovery of RNA-binding protein binding sites
1111 with enhanced CLIP (eCLIP). *Nat. Methods* **13**, 508–514.
1112 **Wang, Y., Arribas-Layton, M., Chen, Y., Lykke-Andersen, J. and Sen, G. L.** (2015).
1113 DDX6 Orchestrates Mammalian Progenitor Function through the mRNA
1114 Degradation and Translation Pathways. *Mol. Cell* **60**, 118–130.
1115 **Wheeler, J. R., Matheny, T., Jain, S., Abrisch, R. and Parker, R.** (2016). Distinct
1116 stages in stress granule assembly and disassembly. *Elife* **5**,.
1117 **Wilbert, M. L., Huelga, S. C., Kapeli, K., Stark, T. J., Liang, T. Y., Chen, S. X., Yan,**
1118 **B. Y., Nathanson, J. L., Hutt, K. R., Lovci, M. T., et al.** (2012). LIN28 Binds
1119 Messenger RNAs at GGAGA Motifs and Regulates Splicing Factor Abundance.
1120 *Mol. Cell* **48**, 195–206.
1121 **Xu, D., Woodfield, S. E., Lee, T. V., Fan, Y., Antonio, C. and Bergmann, A.** (2009).
1122 Genetic control of programmed cell death (apoptosis) in Drosophila. *Fly (Austin).* **3**,
1123 78–90.
1124 **Xu, C., Tang, H.-W., Hung, R.-J., Hu, Y., Ni, X., Housden, B. E. and Perrimon, N.**
1125 (2019). The Septate Junction Protein Tsp2A Restricts Intestinal Stem Cell Activity
1126 via Endocytic Regulation of aPKC and Hippo Signaling. *Cell Rep.* **26**, 670-688.e6.
1127 **Yeo, G. W., Coufal, N. G., Liang, T. Y., Peng, G. E., Fu, X.-D. and Gage, F. H.** (2009).
1128 An RNA code for the FOX2 splicing regulator revealed by mapping RNA-protein
1129 interactions in stem cells. *Nat. Struct. Mol. Biol.* **16**, 130–137.
1130 **Youn, J.-Y., Dyakov, B. J. A., Zhang, J., Knight, J. D. R., Vernon, R. M., Forman-**
1131 **Kay, J. D. and Gingras, A.-C.** (2019). Properties of Stress Granule and P-Body

1132 Proteomes. *Mol. Cell* **76**, 286–294.

1133

1134 **Figure Legends**

1135

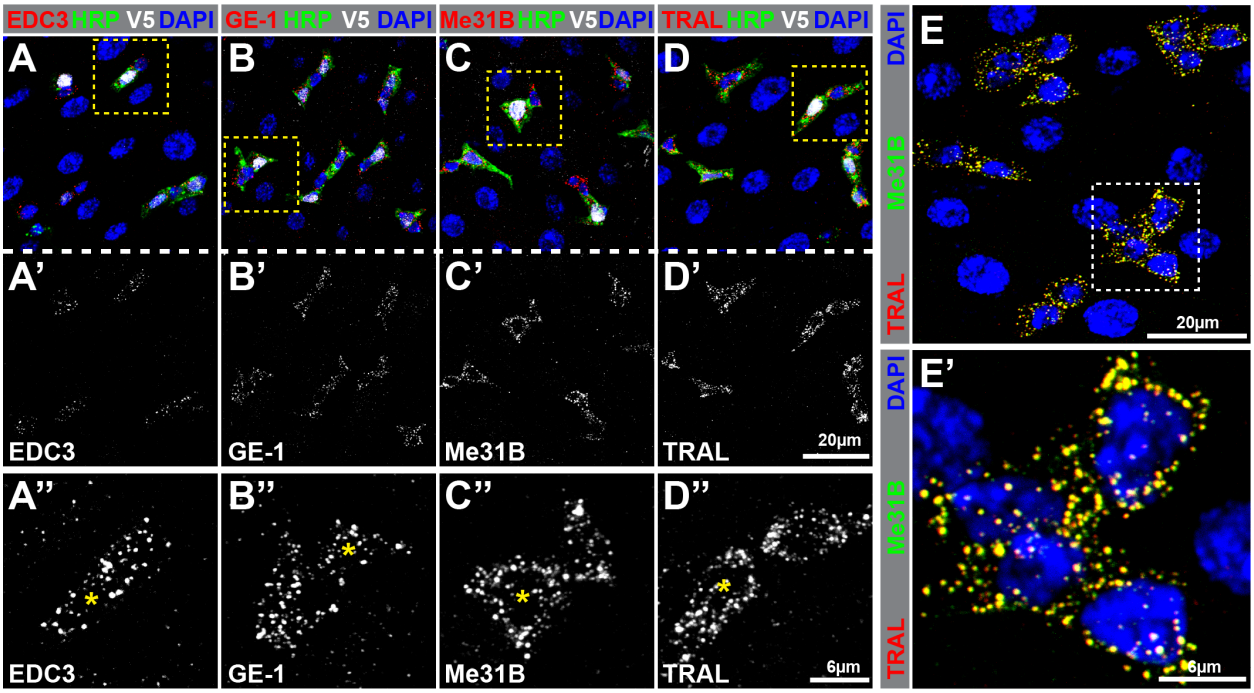

1136 **Figure 1:** P-body proteins are enriched and co-localized in adult intestinal progenitor
1137 cells. (A-D) Confocal micrographs of adult posterior midguts stained for (A) EDC3, (B)
1138 GE-1, (C) Me31B and (D) TRAL. *3Xgbe-smGFP::V5::nls* (white) labels EBs, HRP
1139 (green) labels both EBs and ISCs, and the DNA-dye DAPI (blue) labels all cells. Gray-
1140 scale image of each stained protein is also shown in A'-D'. A"-D" show progenitor cells
1141 marked with yellow dotted outlines in A-D at a higher magnification. Cells labeled with a
1142 yellow asterisk (*) in A"-J" are *gbe*$^{+}$, HRP^{+} EBs while neighboring *gbe*$^{-}$, HRP^{+} cells are
1143 ISCs. (E-E') Fluorescent confocal micrographs of adult posterior midguts stained for
1144 TRAL (red), Me31B (green) and DAPI (blue). E' shows progenitor cells marked with the
1145 white dotted outline on E, at a higher magnification.

1146

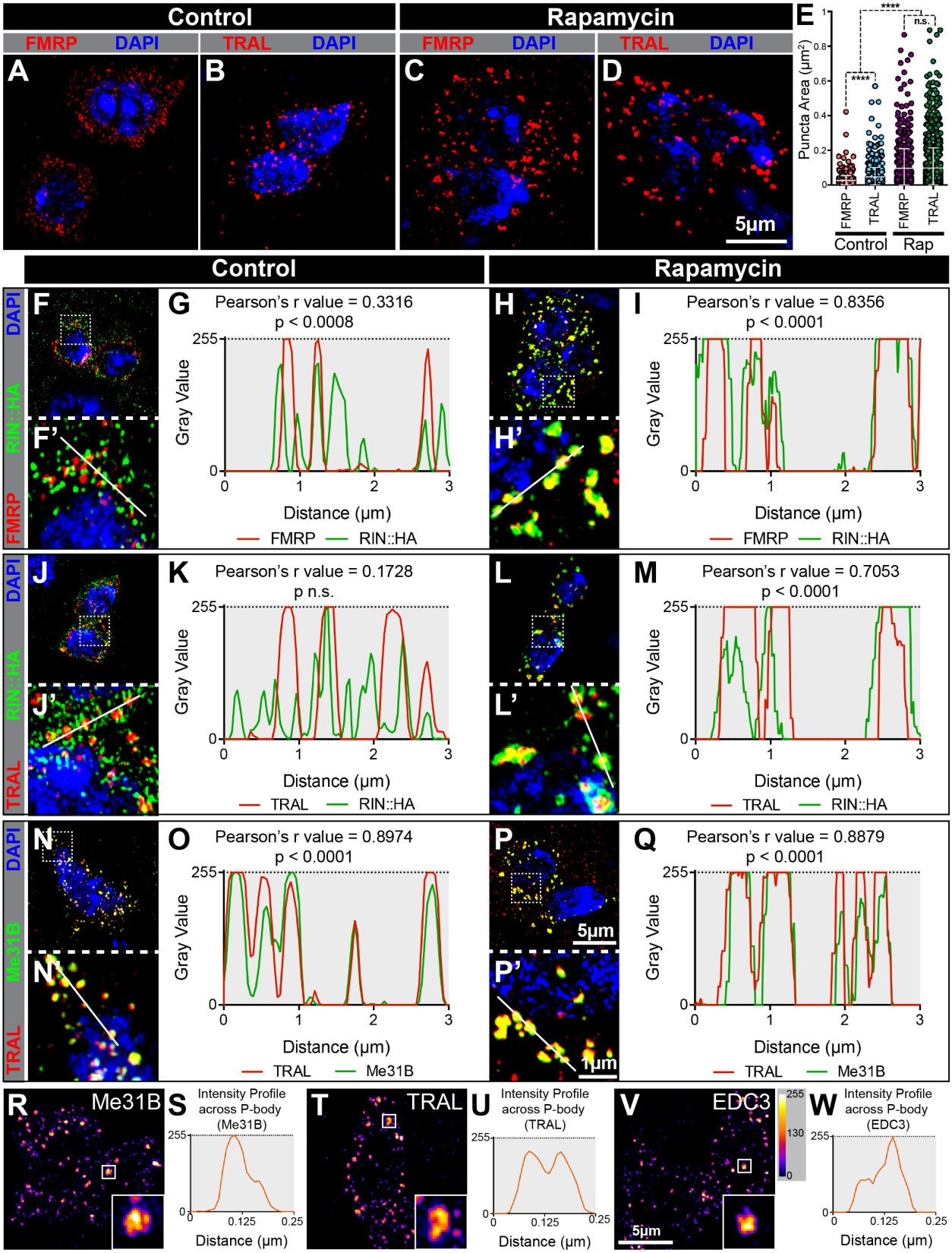

1147 **Figure 2:** P-bodies are a novel population of progenitor mRNPs and localize to IPSGs

following stress. (A-D) Super-resolution micrographs of progenitor cells either treated with (A-B) KRB (control) or (C-D) 1mM rapamycin in KRB, and stained for (A, C) FMRP (red) or (B, D) TRAL (red) and DAPI (blue). (E) Scatter dot plots of FMRP or TRAL puncta area in progenitor cells treated with control or 1mM rapamycin in KRB. Graph shows mean±s.d. ****P<0.0001; n.s., not significant (Kruskal-Wallis test). (F, H, J, L, N, P) Super-resolution micrographs of progenitor cells either treated with (F, J, N) KRB or (H, L, P) 1mM rapamycin in KRB and stained for (F, H) FMRP (red), RIN::HA (green) or (J, L) TRAL (red), RIN::HA (green) or (N, P) TRAL (red), Me31B (green) and DAPI (blue in F, H, J, L, N, P). Figures labeled with a ' show a magnified view of the region marked with white dotted outline in F, H, J, L, N, P. (G, I, K, M, O, Q) Line plots of fluorescent intensity profiles of (G, I) FMRP (red), RIN::HA (green) or (K, M) TRAL (red), RIN::HA (green) or (O, Q) TRAL (red), Me31B (green). The plot shows the pixel-by-pixel gray value of each channel along white lines shown on F', H', J', L', N' or P'. Computed Pearson's r value and the statistical significance of the correlation are given above each plot. (R, T, V) Super-resolution micrographs of progenitor cells that are stained for (R) Me31B, (T) TRAL or (V) EDC3. The ImageJ color lookup table (LUT) "Fire" was used to visualize protein accumulation within granules. Intensity scale represents gray scale intensity of each protein. Insets are enlarged views of boxed regions in the main panels. (S, U, W) Line plots showing fluorescent intensity profiles of (S) Me31B, (U) TRAL or (W) EDC3. The plot shows the pixel-by-pixel gray value of insets shown in R, T and V.

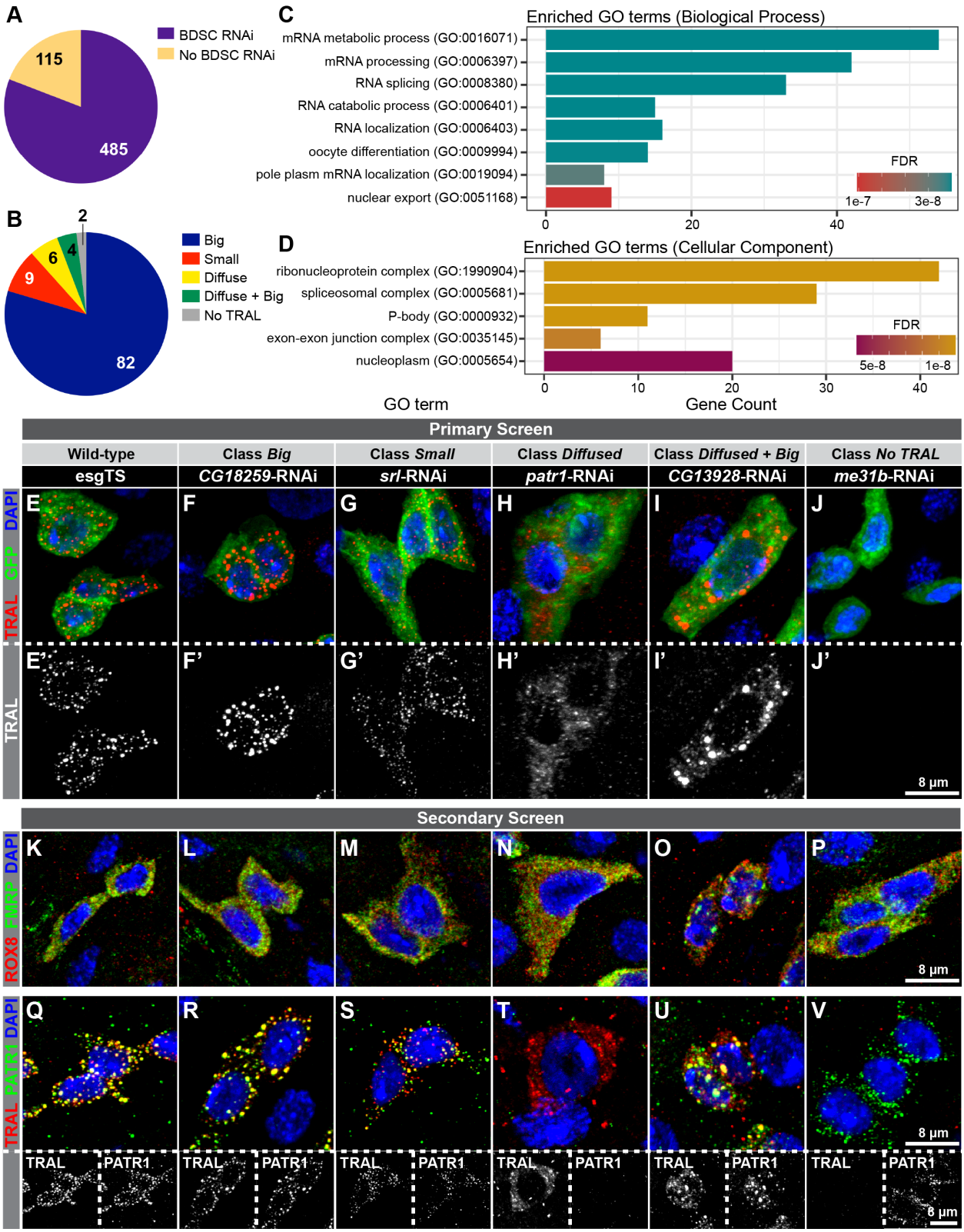

1169 **Figure 3:** A targeted genetic screen identifies genes affecting P-body morphology. (A)
1170 Pie chart showing the number of genes with and without Bloomington *Drosophila* Stock

1171 Center (BDSC) RNAi strains. Note that only genes with BDSC RNAi strains were
1172 analyzed in the screen. (B) Pie chart summarizing phenotypic classes identified during
1173 the primary screen using TRAL as a P-body marker. (C-D) Bar plots visualizing
1174 significantly enriched (C) biological process or (D) cellular component Gene Ontology
1175 (GO) terms (FDR < 0.05) for positive genes. The y-axis represents significantly enriched
1176 GO term and the x-axis represent gene count for each GO term. Color of each bar
1177 represent the FDR. (E-J) Confocal micrographs of intestinal progenitors from (E, K, Q)
1178 control, (F, L, R) *CG18259* RNAi, (G, M, S) *srl* RNAi, (H, N, T) *patr-1* RNAi, (I, O, U)
1179 *CG13928* RNAi or (J, P, V) *me31b* RNAi posterior midguts and stained for (E-J) TRAL
1180 (red), GFP (green) or (K-P) ROX8 (red), FMRP (green) or (Q-V) TRAL (red), PATR-1
1181 (green) and DAPI (blue in E-V). Gray-scale extracts of TRAL staining in panels E-J are
1182 shown in E'-J'. Gray-scale extracts of TRAL and PATR-1 in panels Q-V are shown
1183 below the respective panel.
1184

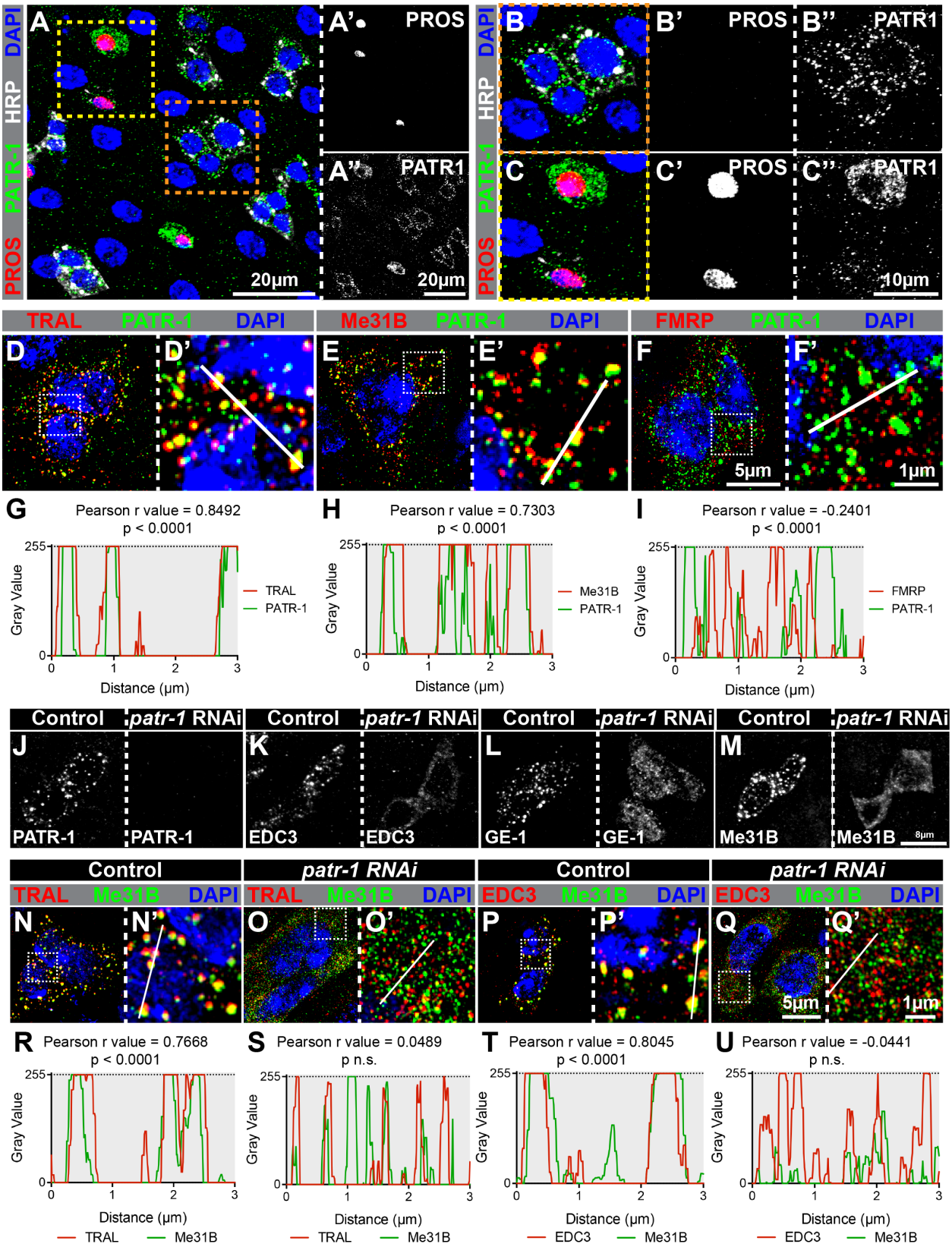
DAPI
HRP
PATR-1
PROS
A
A'
PROS
A''
PATR1
20µm
20µm
B
B'
PROS
B''
PATR1
C
C'
PROS
C''
PATR1
10µm
TRAL PATR-1 DAPI
Me31B PATR-1 DAPI
FMRP PATR-1 DAPI
D
D'
E
E'
F
F'
5µm
1µm
G
Pearson r value = 0.8492
p < 0.0001
Gray Value
Distance (µm)
TRAL
PATR-1
H
Pearson r value = 0.7303
p < 0.0001
Me31B
PATR-1
I
Pearson r value = -0.2401
p < 0.0001
FMRP
PATR-1
Control
patr-1 RNAi
J
PATR-1
K
EDC3
L
GE-1
M
Me31B
8µm
Control
patr-1 RNAi
TRAL Me31B DAPI
EDC3 Me31B DAPI
N
N'
O
O'
P
P'
Q
Q'
5µm
1µm
R
Pearson r value = 0.7668
p < 0.0001
TRAL
Me31B
S
Pearson r value = 0.0489
p n.s.
T
Pearson r value = 0.8045
p < 0.0001
EDC3
U
Pearson r value = -0.0441
p n.s.

1185

1186 **Figure 4:** PATR-1 is an integral component of P-bodies and required for P-body
1187 assembly in intestinal progenitors. (A-C) Confocal micrographs of posterior midguts
1188 stained for PROS (red), PATR-1 (green), HRP (white) and DAPI (blue). Cells marked
1189 with orange and yellow dotted outlines are shown at a higher magnification in B and C
1190 respectively. Note that gray-scale images of PROS and PATR-1 channels are shown in
1191 A'-C' and A''-C'' respectively. (D-F) Super-resolution micrographs of intestinal
1192 progenitors stained for (D-D') TRAL (red), PATR-1 (green) or (E-E') Me31B (red),
1193 PATR-1 (green) or (F-F') FMRP (red), PATR-1 (green) and DAPI (blue in D-F and D'-
1194 F'). (G-I) Line plots showing fluorescent intensity profiles of (G) TRAL (red) or (H)
1195 Me31B (red) or (I) FMRP (red) and PATR-1 (green). The plot shows the normalized
1196 pixel-by-pixel gray value of each channel along white lines shown on D'-F'. Computed
1197 Pearson's r values and the statistical significance of the correlation are given above
1198 each plot. (J-M) Gray-scale confocal images of control (left) or *patr-1* RNAi (right)
1199 progenitor cells that are stained for (J) PATR-1, (K) EDC3, (L) GE-1 or (M) Me31B. (N-
1200 Q) Super-resolution micrographs of (N, P) control or (O, Q) *patr-1* RNAi intestinal
1201 progenitors that are stained for (N-O, N'-O') TRAL (red), Me31B (green) or (P-Q, P'-Q')
1202 EDC3 (red), Me31B (green) and DAPI (blue in N-Q, N'-Q'). (R-U) Line plots showing
1203 fluorescent intensity profiles of (R-S) TRAL (red), Me31B (green) or (T-U) EDC3 (red),
1204 Me31B (green). The plot shows the normalized pixel-by-pixel gray value of each
1205 channel along white lines shown on N'-Q'. Computed Pearson's r values and the
1206 statistical significance of the correlation are given above each plot.
1207

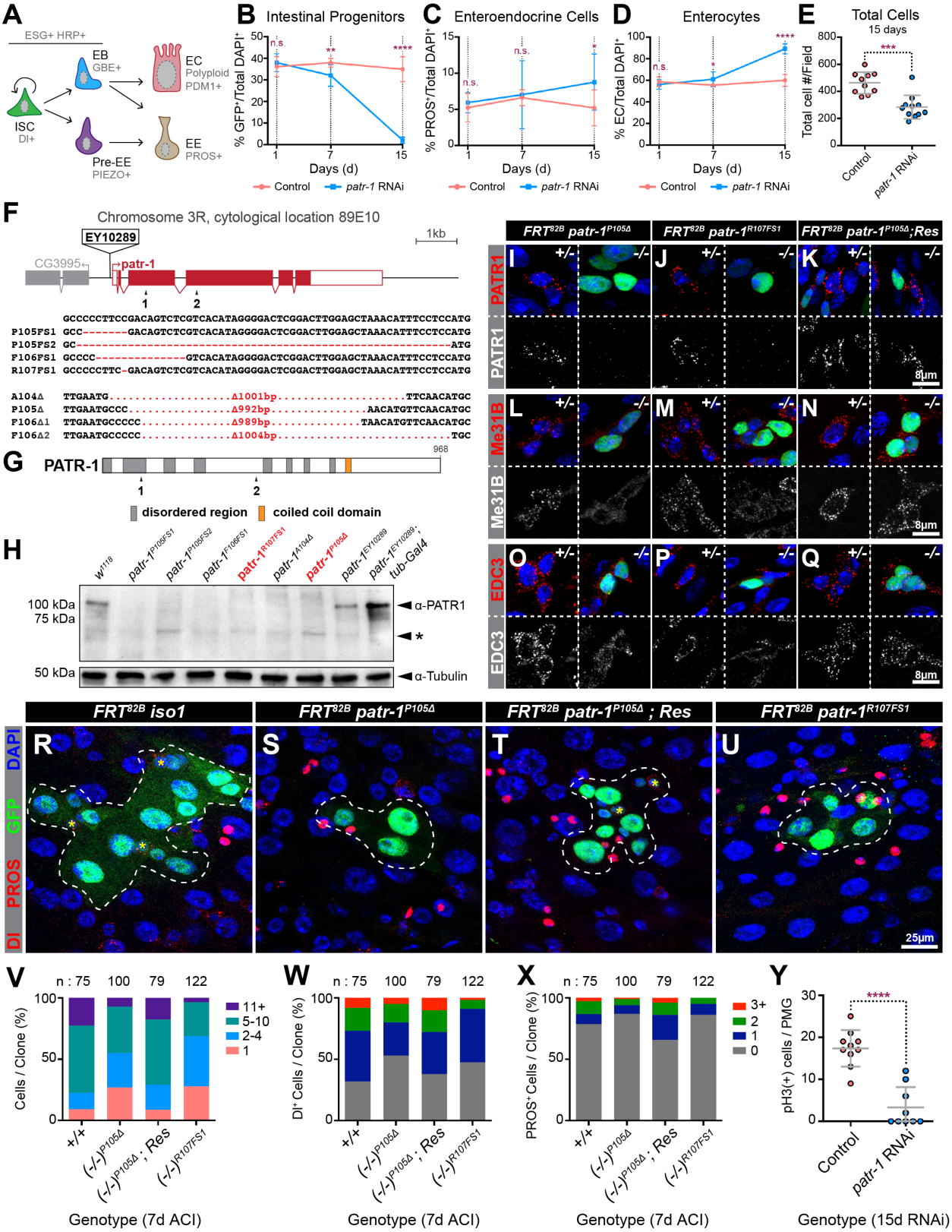
A
ESG+ HRP+
EB
GBE+
ISC
Dl+
Pre-EE
PIEZO+
EC
Polyploid
PDM1+
EE
PROS+
B Intestinal Progenitors
% GFP+/Total DAPI+
Days (d)
Control
patr-1 RNAi
C Enteroendocrine Cells
% PROS+/Total DAPI+
D Enterocytes
% EC/Total DAPI+
E Total Cells
15 days
Total cell #/Field
F
Chromosome 3R, cytological location 89E10
EY10289
1kb
CG3995
patr-1
G
PATR-1
968
disordered region
coiled coil domain
H
w1118
patr-1P105FS1
patr-1P106FS2
patr-1F106FS1
patr-1R107FS1
patr-1A104Δ
patr-1P105Δ
patr-1EY10289
patr-1EY10289; tub-Gal4
100 kDa
75 kDa
50 kDa
α-PATR1
α-Tubulin
FRT82B patr-1P105Δ
FRT82B patr-1R107FS1
FRT82B patr-1P105Δ;Res
PATR1
Me31B
EDC3
8µm
FRT82B iso1
FRT82B patr-1P105Δ ; Res
DAPI
GFP
PROS
Dl
25µm
V
n : 75 100 79 122
Cells / Clone (%)
11+
5-10
2-4
1
+/+
(-/-)P105Δ
(-/-)P105Δ ; Res
(-/-)R107FS1
Genotype (7d ACI)
W
Dl+ Cells / Clone (%)
X
PROS+ Cells / Clone (%)
3+
2
1
0
Y
pH3(+) cells / PMG
Control
patr-1 RNAi
Genotype (15d RNAi)

1208

1209 **Figure 5:** Loss of PATR-1 leads to intestinal progenitor cell loss. (A) Schematic
1210 representation of the intestinal cell types and cell-type specific markers. (B-D) Line plots
1211 showing the normalized (B) intestinal progenitor cell percentage or (C) EE cell
1212 percentage or (D) EC percentage of control (pink) and *patr-1* RNAi (blue) 1, 7 and 15
1213 days after shifting to 29ºC. (E) Dot-plot showing total number of cells per field of view at
1214 15 days after shifting to 29ºC. (F, G) Schematics of the *patr-1* locus (F) and PATR-1
1215 protein, including the location of gRNAs (arrowhead) used to generate new alleles. F
1216 also shows the nucleotide changes associated with the eight newly generated *patr-1*
1217 alleles. (H) Western blot of whole larval extracts derived from w^{1118} (control), the new
1218 *patr-1* alleles, the previously described hypomorphic $patr1^{EY10289}$ allele, and $patr1^{EY10289}$
1219 crossed to tub-Gal4 and probed with PATR-1 (top panel) or Tubulin (bottom panel)
1220 antibodies. The two alleles used in the paper are marked in red. Note that the * shows a
1221 prominent background band detected by the PATR-1 antibody. (I-Q) Confocal
1222 micrographs of intestinal sections harboring (I, L, O) $patr\text{-}1^{P105\Delta}$, (J, M, P) $patr\text{-}1^{R107FS1}$,
1223 or (K, N, Q) rescued $patr\text{-}1^{P105\Delta}$ heterozygous (left and labeled with +/-) and
1224 homozygous mutant (right, labeled with -/- and GFP+) progenitor cells stained for (I-K)
1225 PATR-1 (red) or (L-N) Me31B (red) or (O-Q) EDC3 (red), (I-Q) GFP (green) and (I-Q)
1226 DAPI (blue). (R-U) Representative confocal images of *tub-Gal4, UAS-GFP*-labeled (R)
1227 control, (S) $patr\text{-}1^{P105\Delta}$, (T) rescued $patr\text{-}1^{P105\Delta}$, or (U) $patr\text{-}1^{R107FS1}$ homozygous clones
1228 stained for Dl (red), PROS (red), GFP (green) and DAPI (blue). The size of the clone is
1229 marked by the white dotted line and ISCs in clones are denoted by the yellow asterisks
1230 (*). (V-X) Binned bar plots showing the quantification of (V) total cell, (W) Dl+ ISC or (X)
1231 PROS+ EE cell numbers in *tub-Gal4, UAS-GFP*-labeled control, $patr\text{-}1^{P105\Delta}$, rescued
1232 $patr\text{-}1^{P105\Delta}$, or $patr\text{-}1^{R107FS1}$ homozygous clones analyzed 7 days after clone induction
1233 (ACI). Note that n indicates the total number of clones analyzed for each genotype. (Y)
1234 Dot-plot showing the total number of pH3+ mitotic cells per posterior midgut (PMG) of
1235 control or *patr-1* RNAi flies fed with bleomycin for 24 hours. Rescued (res) strains
1236 harbor the *patr-1* rescuing transgene, *P21M20*.
1237

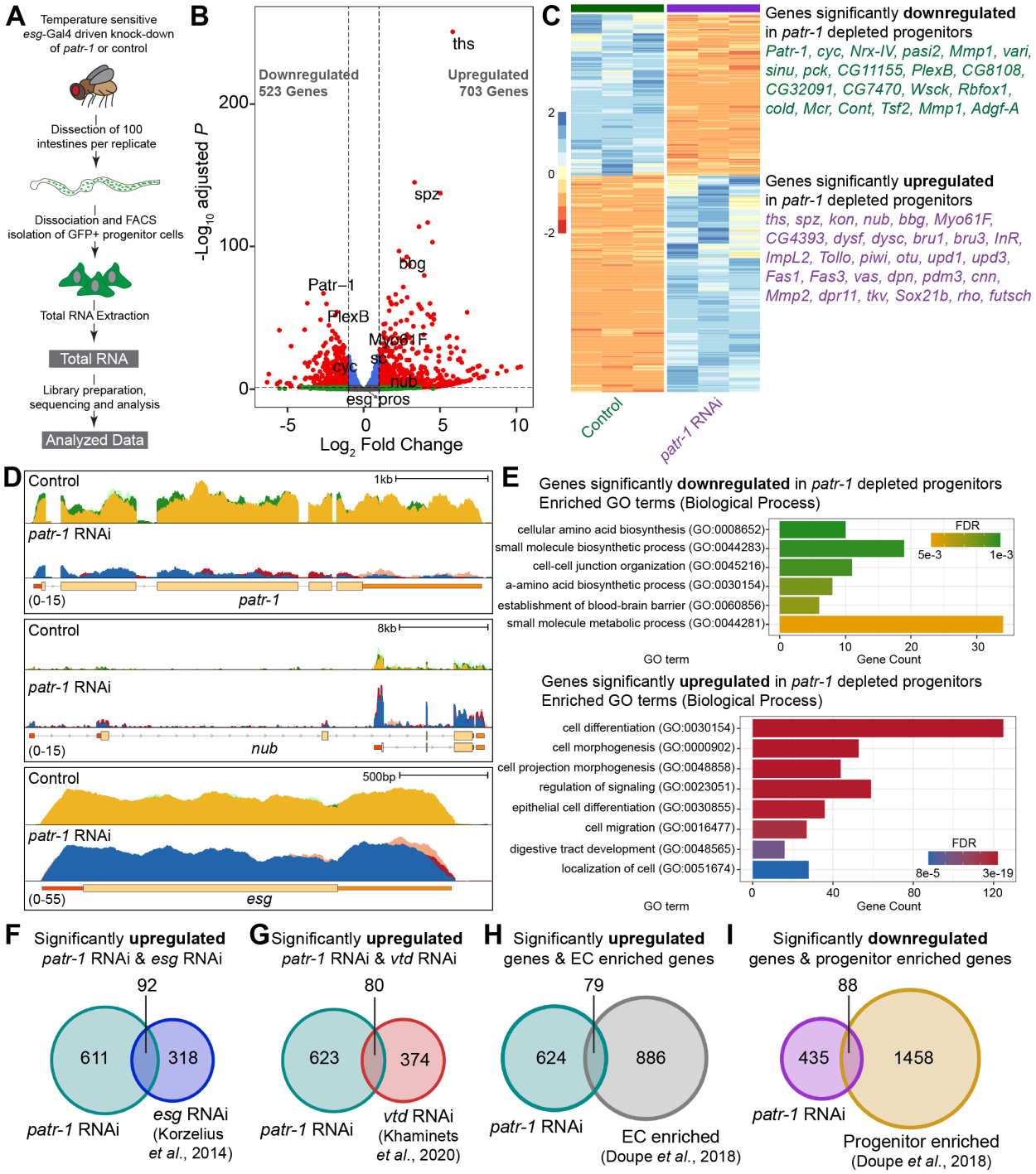

Figure 6: PATR-1 knock-down ectopically upregulates pro-differentiation genes in intestinal progenitors. (A) Schematic representation of the transcriptomic profiling (RNA-seq) of FACS (Fluorescent Activated Cell Sorting) isolated intestinal progenitors of adult female *Drosophila*. (B) Volcano plot of differentially expressed genes from comparison of *patr-1* RNAi with control. Each dot represents a single gene. Blue indicates a false

1243 discovery rate adjusted p-value (FDR) < 0.05 and a Log2 fold change < 1 or > -1. Green
1244 indicates Log_2 fold change > 1 or < -1 and an FDR >= 0.05. Red indicates an FDR <
1245 0.05 and Log_2 fold change > 1 or < -1. (C) Heatmap showing differentially expressed
1246 genes (FDR < 0.05; Log_2 fold change > 1 or < -1) in *patr-1* RNAi compared to control.
1247 Note that gene names of a selected set of upregulated or downregulated genes are
1248 shown. (D) Genome browser tracks of CPM-normalized control and *patr-1* RNAi at the
1249 *patr-1, nub* or *esg* locus of the *Drosophila* genome. Note the three replicates of the
1250 control (yellow, light green and dark green) and the three replicates of the *patr-1* RNAi
1251 (blue, pink and red), have been overlayed for simplicity. (E) Bar plot showing a selected
1252 set of significantly enriched (FDR < 0.05; Fisher's Exact test) Gene Ontology (GO)
1253 terms for genes that are significantly downregulated (FDR < 0.05; Log_2 fold change < -
1254 1) or upregulated (FDR < 0.05; Log_2 fold change > 1) in *patr-1* RNAi compared to
1255 control. (F-I) Venn diagrams showing the overlap of (F) significantly upregulated (FDR <
1256 0.05; Log_2 fold change > 1) genes in *patr-1* RNAi and *esg* RNAi (Korzelius et al., 2014)
1257 or (G) significantly upregulated (FDR < 0.05; Log_2 fold change > 1) genes in *patr-1*
1258 RNAi and *vtd* RNAi (Khaminets et al., 2020) or (H) significantly upregulated (FDR <
1259 0.05; Log_2 fold change > 1) genes in *patr-1* RNAi and EC-enriched genes based on EC
1260 DamID (Doupé et al., 2018) or (I) significantly downregulated (FDR < 0.05; Log_2 fold
1261 change < -1) genes in *patr-1* RNAi and progenitor-enriched genes based on intestinal
1262 progenitor DamID (Doupé et al., 2018).
1263

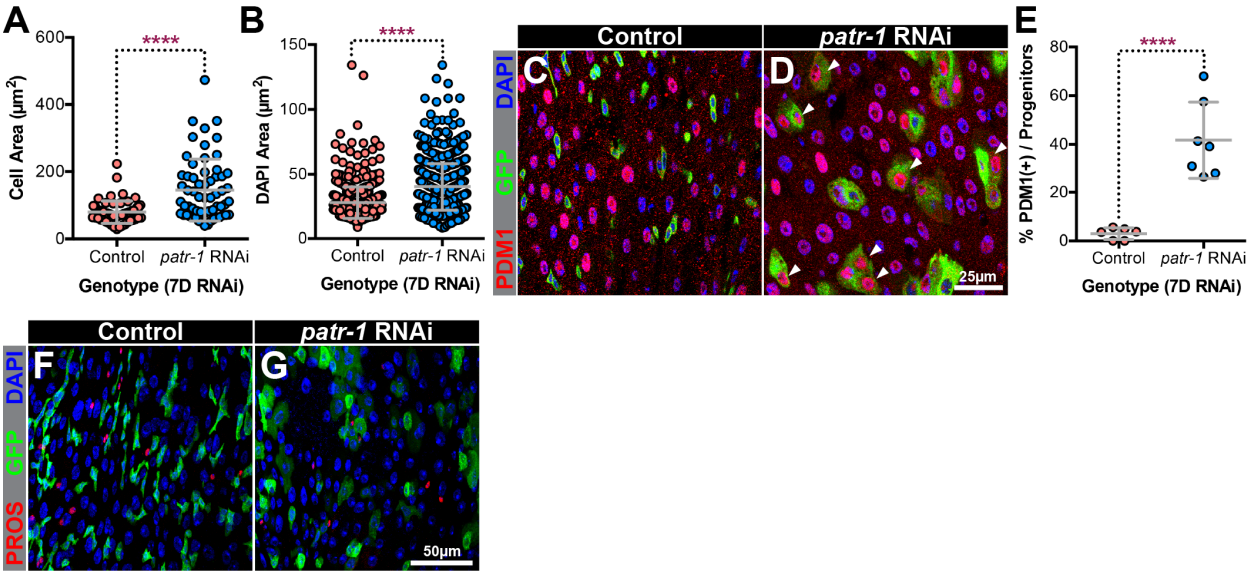

Figure 7: Loss of PATR-1 promotes premature ISC-to-EC-differentiation. (A-B) Dot-plot showing (A) cell area or (B) nuclei area of control and *patr-1* RNAi intestinal progenitors 7 days after shifting to 29ºC. (C-D) Confocal micrographs of intestinal sections from (C) control or (D) *patr-1* RNAi and stained for Pdm1 (red), GFP (green) and DAPI (blue). (E) Dot-plot showing the percentage of GFP+ Pdm1+ cells in control and *patr-1* RNAi 7 days after shifting to 29ºC. (F-G) Confocal micrographs of intestinal sections from (F) control or (G) *patr-1* RNAi and stained for PROS (red), GFP (green) and DAPI (blue).

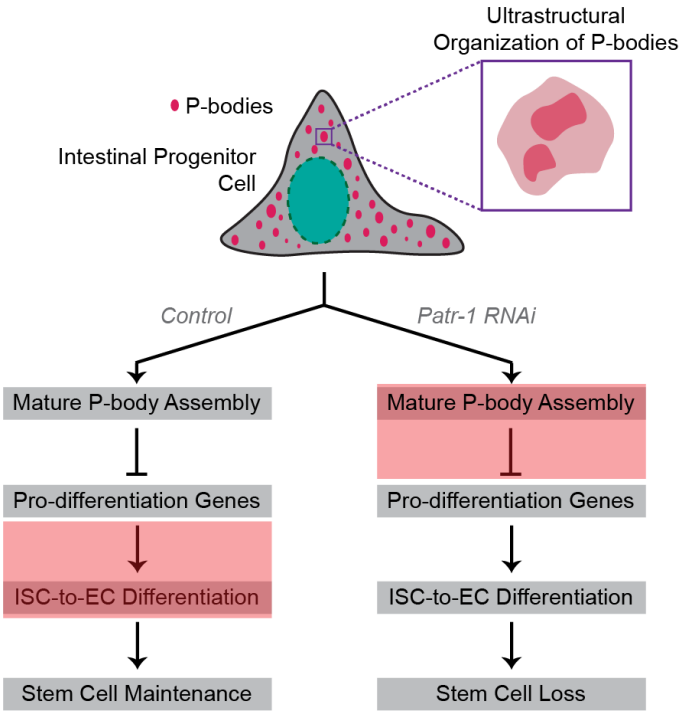

Figure 8: Proposed model of P-body mediated intestinal stem cell maintenance.

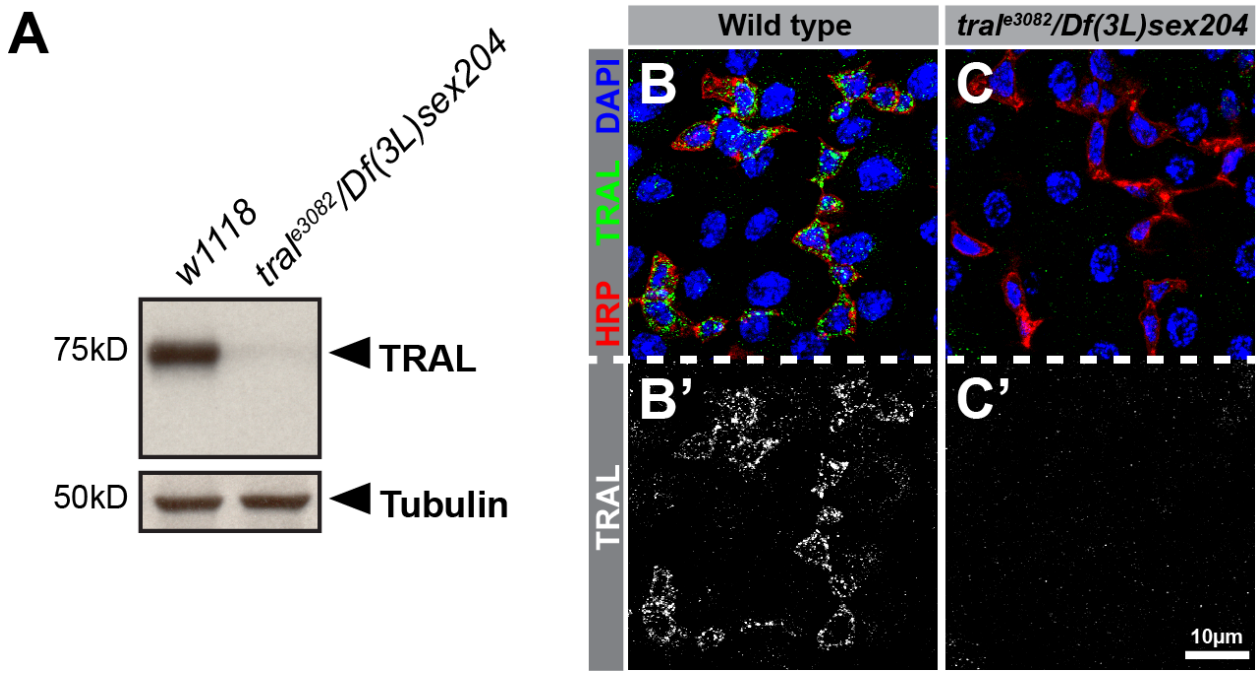

1275 **Figure S1:** Verification of the TRAL antibody. (A) Western blot of *w1118* (control) and
1276 transheterozygous *tral* mutant (*tral*^{e3082}*/Df(3L)sex204*) whole animal extracts probed
1277 with TRAL (top panel) or Tubulin (bottom panel) antibodies. (B-C) Confocal micrographs
1278 of epithelial sections from (B) wildtype (*w1118*) or (C) transheterozygous *tral* mutant
1279 (*tral*^{e3082}*/Df(3L)sex204*) intestines stained for HRP (red), TRAL (green in B-C, white in
1280 B'-C') and DAPI (blue). Note that *tral* mutant intestinal progenitors have no detectable
1281 TRAL staining.
1282

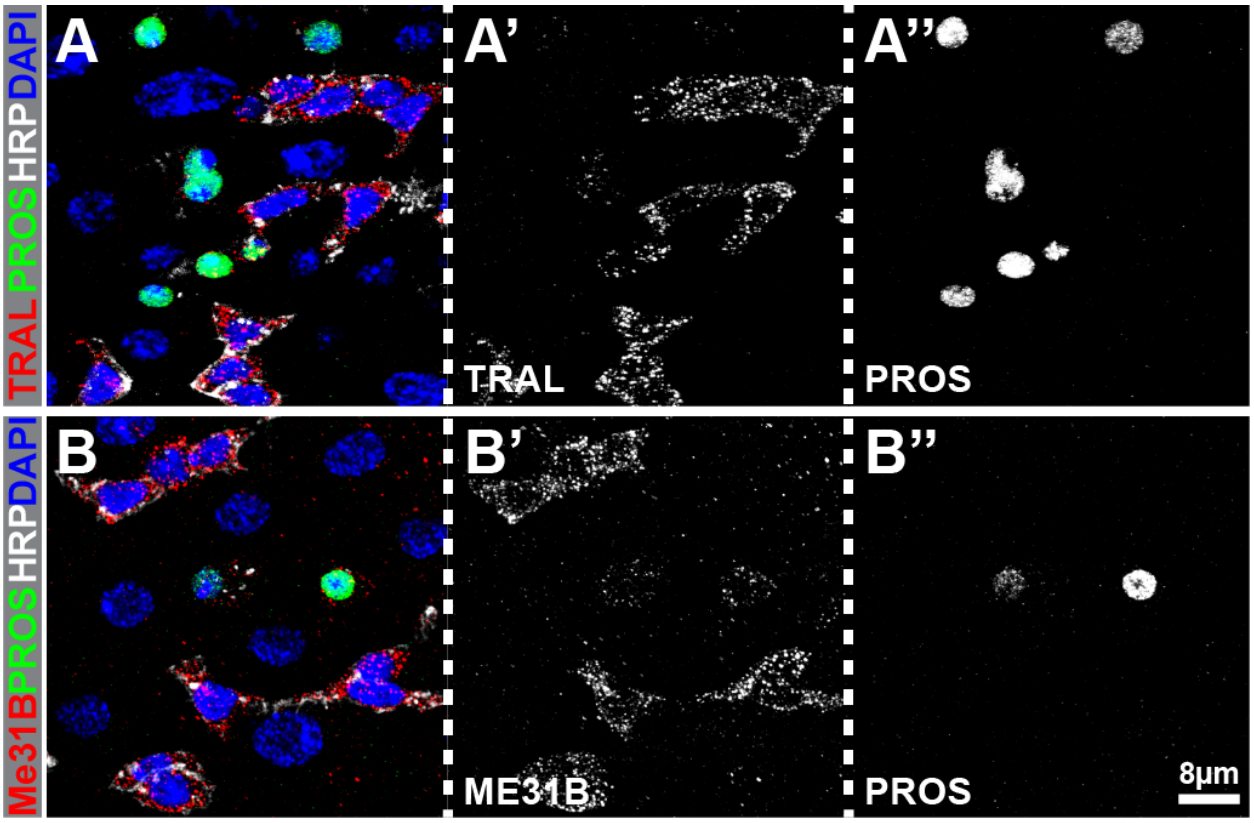

1283 **Figure S2:** P-bodies are enriched in intestinal progenitors, but rarely observed in some
1284 EEs. (A-B) Confocal micrographs of intestinal sections stained for (A) TRAL (red) or (B)
1285 Me31B (red), (A-B) prospero (green), (A-B) HRP (white) and (A-B) DAPI. While TRAL
1286 and Me31B granules are readily observed in HRP+ intestinal progenitors only some
1287 prospero+ EEs have detectable TRAL or Me31B expression.
1288

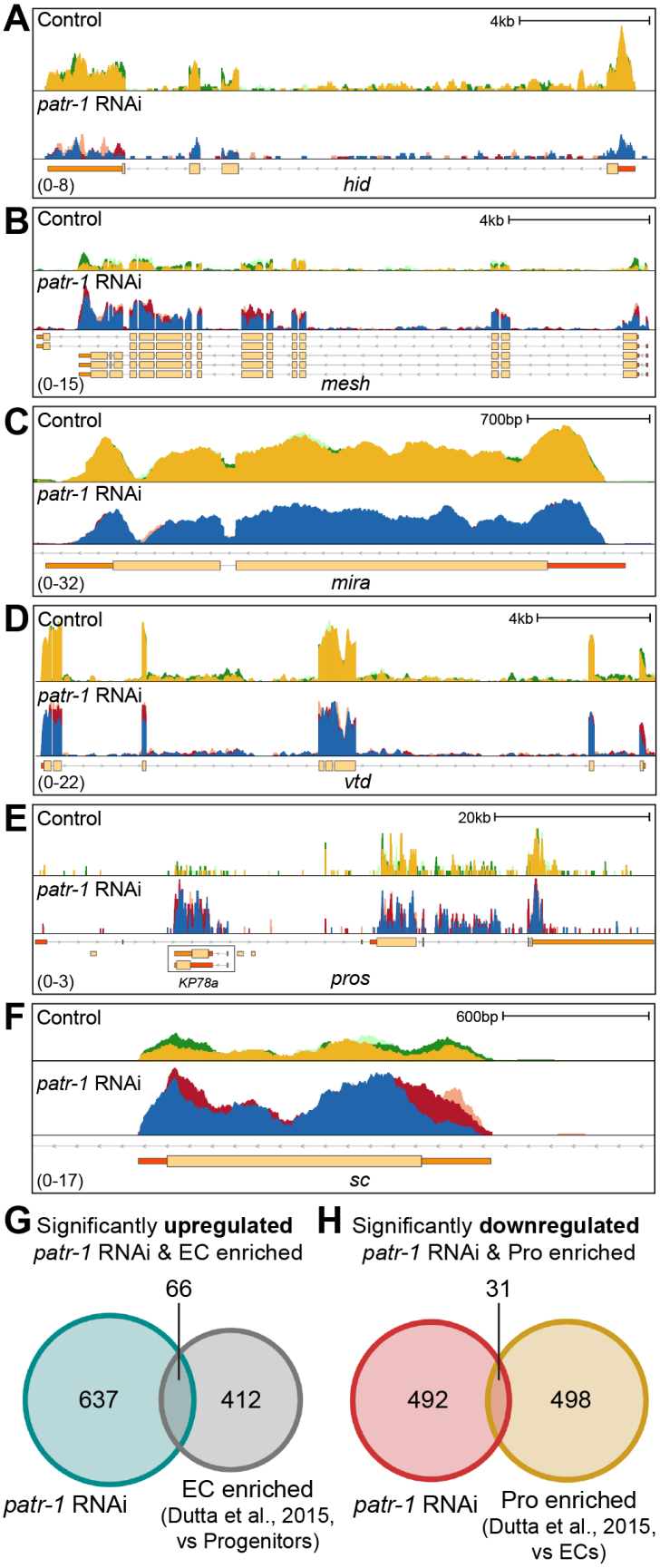

Figure S3: Gene expression changes associated with *patr-1* RNAi. (A-F) Genome browser tracks of CPM-normalized control and *patr-1* RNAi at the (A) *hid,* (B) *mesh,* (C) *mira,* (D) *vtd,* (E) *pros* or (F) *sc* locus of the *Drosophila* genome. Note the three replicates of the control (yellow, light green and dark green) and the three replicates of the PATR-1 RNAi (blue, pink and red), have been overlayed for simplicity. (G-H) Venn diagrams showing the overlap of (G) significantly upregulated (FDR < 0.05; Log_2 fold change > 1) genes in *patr-1* RNAi and EC-enriched genes or (H) significantly downregulated (FDR < 0.05; Log_2 fold change < -1) genes in *patr-1* RNAi and progenitor enriched genes based on Dutta et al. 2015.

1312 **Supplementary Tables**

1313

1314 **Table S1: Fly strains used in this study**

Figure	Panels	Genotypes of flies used in each panel
Fig. 1	A-D	*gbe-smGFP::V5::nls / +*
	E	*w1118*
Fig. 2	A-E, R-W	*w1118*
	F-P	*HA::rin / +*
Fig. 3	E	*esg-Gal4 UAS-GFP tubGal80^{ts} / +*
	F	*esg-Gal4 UAS-GFP tubGal80^{ts} / P{y[+t7.7] v[+t1.8]=TRiP.HMJ22374}attP40 (BL58288)*
	G	*esg-Gal4 UAS-GFP tubGal80^{ts} / + ; P{y[+t7.7] v[+t1.8]=TRiP.HMS00857}attP2 (BL33914) / +*
	H	*esg-Gal4 UAS-GFP tubGal80^{ts} / + ; P{y[+t7.7] v[+t1.8]=TRiP.HMS01144}attP2/TM3, Sb[1] (BL34667) / +*
	I	*esg-Gal4 UAS-GFP tubGal80^{ts} / + ; P{y[+t7.7] v[+t1.8]=TRiP.JF03061}attP2 (BL28646) / +*
	J	*esg-Gal4 UAS-GFP tubGal80^{ts} / + ; P{y[+t7.7] v[+t1.8]=TRiP.HM05052}attP2 (BL28566) / +*
	K, Q	*{mira -KDRT>-dSTOP-KDRT>-Gal4^{1438}}attP40, P{tubP-Gal80[ts]}20 / + ; {CG10116-KD::PEST^{1107}}attP2 / +*
	L, R	*{mira -KDRT>-dSTOP-KDRT>-Gal4^{1438}}attP40, P{tubP-Gal80[ts]}20 / P{y[+t7.7] v[+t1.8]=TRiP.HMJ22374}attP40 (BL58288) ; {CG10116-KD::PEST^{1107}}attP2 / +*
	M, S	*{mira -KDRT>-dSTOP-KDRT>-Gal4^{1438}}attP40, P{tubP-Gal80[ts]}20 / + ; {CG10116-KD::PEST^{1107}}attP2 / P{y[+t7.7] v[+t1.8]=TRiP.HMS00857}attP2 (BL33914)*
	N, T	*{mira -KDRT>-dSTOP-KDRT>-Gal4^{1438}}attP40, P{tubP-Gal80[ts]}20 / + ; {CG10116-KD::PEST^{1107}}attP2 / P{y[+t7.7] v[+t1.8]=TRiP.HMS01144}attP2 (BL34667)*
	O, U	*{mira -KDRT>-dSTOP-KDRT>-Gal4^{1438}}attP40, P{tubP-Gal80[ts]}20 / + ; {CG10116-KD::PEST^{1107}}attP2 / P{y[+t7.7] v[+t1.8]=TRiP.JF03061}attP2 (BL28646)*
	P, V	*{mira -KDRT>-dSTOP-KDRT>-Gal4^{1438}}attP40, P{tubP-Gal80[ts]}20 / + ; {CG10116-KD::PEST^{1107}}attP2 / P{y[+t7.7] v[+t1.8]=TRiP.HM05052}attP2 (BL28566)*
Fig. 4	A-I	*w1118*
	J-M	*esg-Gal4 UAS-GFP tubGal80^{ts} / +*
	J-M	*esg-Gal4 UAS-GFP tubGal80^{ts} / + ; P{y[+t7.7] v[+t1.8]=TRiP.HMS01144}attP2 (BL34667) / +*
	N, P, R, T	*esg-Gal4 UAS-GFP tubGal80^{ts} / +*
	O, Q, S, U	*esg-Gal4 UAS-GFP tubGal80^{ts} / + ; P{y[+t7.7] v[+t1.8]=TRiP.HMS01144}attP2 (BL34667) / +*
Fig. 5	B-E, Y	*esg-Gal4 UAS-GFP tubGal80^{ts} / +*
	B-E, Y	*esg-Gal4 UAS-GFP tubGal80^{ts} / + ; P{y[+t7.7] v[+t1.8]=TRiP.HMS01144}attP2 (BL34667) / +*
	H	*w1118*
	H	*patr-1^{P105FS1}*
	H	*patr-1^{P105FS2}*
	H	*patr-1^{P106FS1}*
	H	*patr-1^{P107FS1}*

	H	*patr-1$^{P104\Delta}$*
	H	*patr-1$^{P105\Delta}$*
	H	*patr-1^{EY10289}*
	H	*patr-1^{EY10289} ; tub-Gal4 / +*
	I, L, O, S, V-X	*hsFLP^{12} , tubGAL4, UAS-GFP / + ; P{lin-28 13kb::mCherry}attP40 / + ; FRT^{82B} tubP-GAL80^{LL3}/ FRT82B patr-1$^{P105\Delta}$*
	J, M, P, U-X	*hsFLP^{12} , tubGAL4, UAS-GFP / + ; P{lin-28 13kb::mCherry}attP40 / + ; FRT^{82B} tubP-GAL80^{LL3}/ FRT82B patr-1^{R107FS1}*
	K, N, Q, T, V-X	*hsFLP^{12} , tubGAL4, UAS-GFP / + ; P{lin-28 13kb::mCherry}attP40 / P21M20 ; FRT^{82B} tubP-GAL80^{LL3}/ FRT82B Patr-1$^{P105\Delta}$*
	R, V-X	*hsFLP^{12} , tubGAL4, UAS-GFP / + ; P{lin-28 13kb::mCherry}attP40 / + ; FRT^{82B} tubP-GAL80^{LL3}/ FRT82B iso1*
Fig. 6	A-I	*esg-Gal4 UAS-GFP tubGal80^{ts} / +*
	A-I	*esg-Gal4 UAS-GFP tubGal80^{ts} / + ; P{y[+t7.7] v[+t1.8]=TRiP.HMS01144}attP2/ (BL34667) / +*
Fig. 7	A-G	*esg-Gal4 UAS-GFP tubGal80^{ts} / +*
	A-G	*esg-Gal4 UAS-GFP tubGal80^{ts} / + ; P{y[+t7.7] v[+t1.8]=TRiP.HMS01144}attP2/ (BL34667) / +*
Fig. S1	A-C	*w1118*
	A-C	*tral^{e3082} / Df(3L)sex204 (BL9337)*
Fig. S2	A-B	*w1118*
Fig. S3	A-H	*esg-Gal4 UAS-GFP tubGal80^{ts} / +*
	A-H	*esg-Gal4 UAS-GFP tubGal80^{ts} / + ; P{y[+t7.7] v[+t1.8]=TRiP.HMS01144}attP2/ (BL34667) / +*

1315

1316